


Detection of meteoroid impacts by the Geostationary Lightning Mapper on the GOES-16 satellite

Peter JENNISKENS ^{1,2*}, Jim ALBERS³, Clemens E. TILLIER³, Samantha F. EDGINGTON³, Randolph S. LONGENBAUGH², Steven J. GOODMAN⁴, Scott D. RUDLOSKY⁵, Alan R. HILDEBRAND⁶, Lincoln HANTON⁶, Fabio CICERI⁶, Richard NOWELL⁷, Esko LYYTINEN⁸, Donald HLADIUK⁹, Dwayne FREE¹⁰, Nicholas MOSKOVITZ¹¹, Len BRIGHT¹¹, Christopher O. JOHNSTON¹², and Eric STERN²

¹SETI Institute, Carl Sagan Center, Mountain View, California 94043, USA

²NASA Ames Research Center, Moffett Field, California 94035, USA

³Lockheed Martin, Palo Alto, California 94304, USA

⁴GOES-R Program Office, NASA GSFC, Code 410, Greenbelt, Maryland 20771, USA

⁵NOAA/NESDIS/STAR, College Park, Maryland 20740, USA

⁶Department of Geoscience, University of Calgary, Calgary, Alberta T2N 1N4, Canada

⁷College of the Rockies, 2700 College Way, Cranbrook, British Columbia V1C 5L7, Canada

⁸Kehäkukantie 3 B, 00720 Helsinki, Finland

⁹28 Sunmount Rise SE, Calgary, Alberta T2X 2C4, Canada

¹⁰Spalding Allsky Camera Network, SkySentinel, LLC (SSL), Melbourne, Florida 32940, USA

¹¹Lowell Observatory, Flagstaff, Arizona 86001, USA

¹²NASA Langley Research Center, Hampton, Virginia 23681, USA

*Corresponding author. E-mail: petrus.m.jenniskens@nasa.gov

(Received 07 March 2018; revision accepted 22 May 2018)

Abstract—Bolides are detected by the Geostationary Lightning Mapper onboard the GOES-16 weather satellite, which takes images of Earth at a rate of 500 Hz in a 1.1 nm wide pass band centered on 777.4 nm wavelength. Ten case studies are discussed. These initial results were obtained using the Level 0 data received during the nonoperational in-orbit postlaunch test period. GLM positions and timings are sufficiently accurate to assist in trajectory and orbit reconstruction. GLM samples the light curve nearly completely, unaffected by onboard and downlink processes tailored to lightning data. Sufficient data on the instantaneous background scene are provided to reconstruct the baseline drift in the brightest pixels. The agreement to within a factor of 2–3 between measured total radiated energy from GLM and that derived from other space-borne observations implies that during the bolide's peak brightness the GLM pass band is dominated by continuum emission, rather than O I line emission. The reported flux is corrected for angle-from-nadir shifts in the central wavelength of the pass band, which overestimates continuum flux by only up to 20% for most of the GLM field of view, but more so if the bolide is observed far from nadir. Assuming a 6000 K blackbody spectrum, GLM is able to detect bolides with peak visual magnitude (at a normalized 100 km distance) brighter than about –14 in nighttime, and slightly brighter in daytime.

INTRODUCTION

Tagliaferri et al. (1998), 20 years ago, foresaw the practical use of NASA's proposed space-based Lightning Mapper for the detection of meteoroid impacts (Goodman

et al. 1988; Christian et al. 1989). This instrument would image the Earth from geostationary orbit and detect the scattered light of lightning over ~8 km sized areas at a rate of ~500 frames per second. At the time, the instrument's planned launch ran against payload limitations and was

envisioned for deployment only on a future Geostationary Observational Environmental Satellite (GOES) weather satellite (Goodman et al. 2013).

Until now, meter-sized meteoroid impacts were recorded almost exclusively by visible light transient radiometers and by scanning infrared sensors as part of the nuclear burst monitoring system onboard a network of geostationary satellites that are operated by the U.S. Government Department of Defense for military missions (USG satellites) (Tagliaferri et al. 1998). Time, position, and altitude of peak brightness, total radiated energy, as well as the entry speed and track vector (only when two or more burst locators detect the bolide) are routinely reported at a NASA JPL website (<https://cneos.jpl.nasa.gov/fireballs/>). These data have been used to evaluate the influx of meter-sized bodies in the Earth's atmosphere (e.g., Nemtchinov et al. 1997; Brown et al. 2002a, 2016; Gi and Brown 2017). Other space-based narrow-field scanning sensors have been used to image the debris cloud of asteroid impacts (e.g., Hildebrand et al. 2006; Borovicka and Charvát 2009; Miller et al. 2013).

Thirteen radiometer light curves were published from bolides in the period 1988–2008 (Table 1), which demonstrated their usefulness in evaluating the fragmentation behavior of small asteroids (Tagliaferri et al. 1998; Pedersen et al. 2001; Brown et al. 2002b, 2002c, 2004; Klekociuk et al. 2005). The manner in which kinetic energy is deposited in the atmosphere, resulting in airbursts, is in large part determined by how the meteoroid fragments upon entry. Little is known about the fragmentation behavior of the different meteorite types from various source regions. NASA's Asteroid Threat Assessment Project at Ames Research Center is developing tools to evolve light curve models to derive meteoroid strength, ablation, and fragmentation behavior from these data (e.g., Register et al. 2017; Wheeler et al. 2017).

Interesting differences were noticed between satellite-detected light curves and those derived from video cameras on the ground (Pedersen et al. 2001; Klekociuk et al. 2005), which can provide insight into processes of ablation and fragmentation if those differences are caused by a different spectral responsivity of the sensors. At visible and near-IR wavelengths, bolides have strong neutral oxygen and nitrogen atom line emissions (mostly at wavelengths 740–880 nm); molecular bands of the First Positive system of molecular nitrogen (560–780 nm); as well as line emissions from ablated metal atoms (mostly <600 nm), bands of metal oxides (e.g., CaO: 550–650 nm), and continuum emission from free-free radiation and gray body emission from solid particles (e.g., Borovicka 2005; Jehin et al. 2007; Borovicka and Berezhnoy 2016).

Unlike past bolide photometers, the Geostationary Lightning Mapper (GLM) instrument measures emissions

in a narrow ~1.1 nm wide pass band centered on the neutral oxygen 777.4 nm line. The first of four instruments was launched on November 19, 2016 as one of the six scientific instruments on the new-generation NOAA GOES-R weather satellite series (Goodman et al. 2013). The first Level 0 data were collected in January 2017 with a planned 1-year of postlaunch instrument and product testing. During much of 2017, the ground processing algorithms were refined to achieve a well-calibrated and -validated Level 2 operational data product having 20 s or better latency starting in January 2018. In December 2017, this first satellite, now named GOES-16, was placed into operations at 75.2W as the replacement for the GOES-East satellite. The second satellite in the series, GOES-S, launched on March 1, 2018 and will replace the current GOES-West satellite at 137W, completing the refresh of NOAA's geostationary satellite constellation providing routine monitoring of high impact environmental phenomena across the western hemisphere.

Despite its narrow pass band, we realized early that the new GLM had the capacity to potentially detect bolides. Here, we will show that GLM does detect bolides by discussing an incomplete list of seven bolides and three fireballs that occurred in the field of view over the course of less than a year during the commissioning phase. Results are compared to other space-borne and ground-based video observations in order to evaluate the detection threshold and the data processing procedures in order to determine whether we can back out physical knowledge from GLM data.

EXPERIMENTAL METHODS

The GLM records transient light events at a rate of 500 frames per second, corresponding to a 2 ms frame exposure (GOES-R Data Book 2018). Figure 1 shows an example whole-globe image, with superposed 20 min of accumulated lightning detections.

The sensor is a nadir-pointed single-channel near-IR CCD focal plane of 1372×1300 pixels, with a 14-bit dynamic range of the optical intensity digitization. The spatial resolution in the images is nearly uniform at about 8 km/pixel in nadir and 12 km/pixel at the corner of the field of view, due to a variable pixel size on the detector ($30 \times 30 \mu\text{m}$ at nadir, reducing in steps to the smallest $20 \times 24 \mu\text{m}$ near the edge). The mapping accuracy is about ± 5 km, corresponding to the error in latitude and longitude position at the center of the pixel.

The 134 mm f1.2 lens has a field of view of $\pm 8^\circ$ (aperture diameter 110 mm) and is clipped just inside the Earth limb. Coverage from the GOES-East position at 75°W is currently between about longitude 18° – 132°W and latitude 54°S – 54°N , and will be extended

Table 1. U.S. government–detected bolides for which light curves have been published.

Date	Time (UTC)	Location	Duration (s)	Lat. (+N, °)	Long. (+E, °)	Yield (kt)	Meteorite type	Ref.
April 15, 1988	03:03:11	Indonesia	1.9	−4.1	+124.3	14	–	(a)
October 01, 1990	03:51:47	West Pacific	1.9	+7.5	+142.8	5.2	–	(a)
October 04, 1991	09:22:47	Svalbard	1.6	+78.7	+6.3	1.4	–	(a)
February 01, 1994	22:38:09	Marshall Islands	2.1	+2.7	+164.1	30	–	(b)
May 29, 1994	09:30:58	U.K.	0.7	+58.8	+2.3	1	–	(c)
June 15, 1994	00:02:26	St. Robert, Canada	0.5	+45.0	−73.5	1.3	H5	(d)
December 12, 1997	08:15:55	Greenland	1.6	+62.7	−49.9	0.73	–	(e)
January 01, 2000	16:43:42	Tagish Lake, Can.	9.5	+60.3	−134.6	2.4	C2	(f)
May 06, 2000	11:51:52	Moravka, Czech R.	2.2	+49.9	+18.4	0.098	H5	(g)
June 02, 2002	04:28:22	Mediterranean	3.3	+34.0	+21.0	8.8	–	(h)
March 27, 2003	05:50:26	Park Forest, USA	1.0	+41.4	−87.7	0.41	L5	(i)
September 03, 2004	12:07:27	Antarctica	5.3	−67.7	+18.2	13	–	(j)
July 23, 2008	14:45:25	Tajikistan	3.7	+38.6	+68.0	0.36	–	(k)

References: (a) Tagliaferri et al. (1998); (b) Tagliaferri et al. (1995); McCord et al. (1995); (c) Ens et al. (2012); (d) Brown et al. (1996); (e) Ceplecha et al. (1999); Pedersen et al. (2001); (f) Brown et al. (2002c); (g) Borovicka et al. (2003); (h) Brown et al. (2002a); (i) Brown et al. (2004); (j) Klekociuk et al. (2005); (k) Konovalova et al. (2013).

westward as the second GLM on the GOES-S satellite comes online in the GOES-West position at 137°W in late 2018.

The spectral pass band is only ~1.1 nm wide and centered on the 777.4 nm O I triplet of atomic lines. This is to ensure, in conjunction with spatial and temporal filtering, that lightning can be detected against the bright daytime cloud background. Spectral responsivity (how much current comes out of the device per incoming photon of a given energy and wavelength) is plotted in Fig. 2. Compared to that of the broadband USG satellite sensor and that of modern digital and video cameras, GLM is particularly suited to isolate the O I line emission, but will also detect metal atom lines and continuum emission in that narrow pass band.

The full CCD frames are processed onboard by tracking and subtracting the scene background in a known manner. When the residual pixel brightness in a frame exceeds a threshold of 4.5 times the standard deviation of the instrument noise in that pixel, a thresholding event is declared and that residual pixel position and brightness is down-linked at a rate of ~7.7 Mbps (Level 0 data) or $\geq 10^5$ events per second. Even though there is only a 1 in 3.4 million chance of a noise event being registered, the large number of pixels in each frame and 500 frames per second results in several thousand noise false events per second (GOES-R Data Book 2018).

The intensity of the cloud scene background at each pixel is updated with each new frame in a well-defined manner. The computed value is that of an exponential moving average, with an adjusted time constant (k). The time constant is configurable and currently set at $k = 64$ frames, the highest value. The maximum change in

background from frame to frame is also configurable and is currently set at two counts. The value of the background's five most significant bits is communicated to the ground in each event report. Note that the full bit depth is not transmitted in order to save downlink bandwidth.

Detections are geolocated, time-tagged, and intensity calibrated. The raw events (one record per pixel) are part of the Level 0 data stream and are processed on the ground into Level 1/1b and Level 2 products by checking the threshold crossings and by removing false detections from, among others, cloud scene motion, shot-noise, and solar glint. Level 1/1b data have, among others, a coherency filter applied that selects events that are coherent in time and space and removes signals that appear to be noise. In Level 2 data, the individual pixel threshold crossing “events” are clustered into “groups” (i.e., strokes) and “flashes” (i.e., network of strokes) by the Lightning Cluster-Filter Algorithm and transmitted to the user with <20 s latency (Mach et al. 2007).

In addition, a single full image is downloaded every 2.5 min, containing the cloud background intensity value at each pixel calculated for that moment in time. That image is used to refine the geodetic location of each GLM pixel. The geolocation of these events assumes that the lightning emanates from a “lightning ellipsoid,” an imaginary surface several kilometers above the ground at the typical altitude of cumulonimbus cloud tops: a tropopause-centered ellipsoid at ~16 km altitude at the equator and ~6 km at the pole (Christian and Goodman 1987). With the Earth ellipsoid mathematically defined as having dimensions 6378.137×6356.752 km (World Geodetic System [WGS 84] ellipsoid reference used by Global Positioning System [GPS]), the lightning ellipsoid

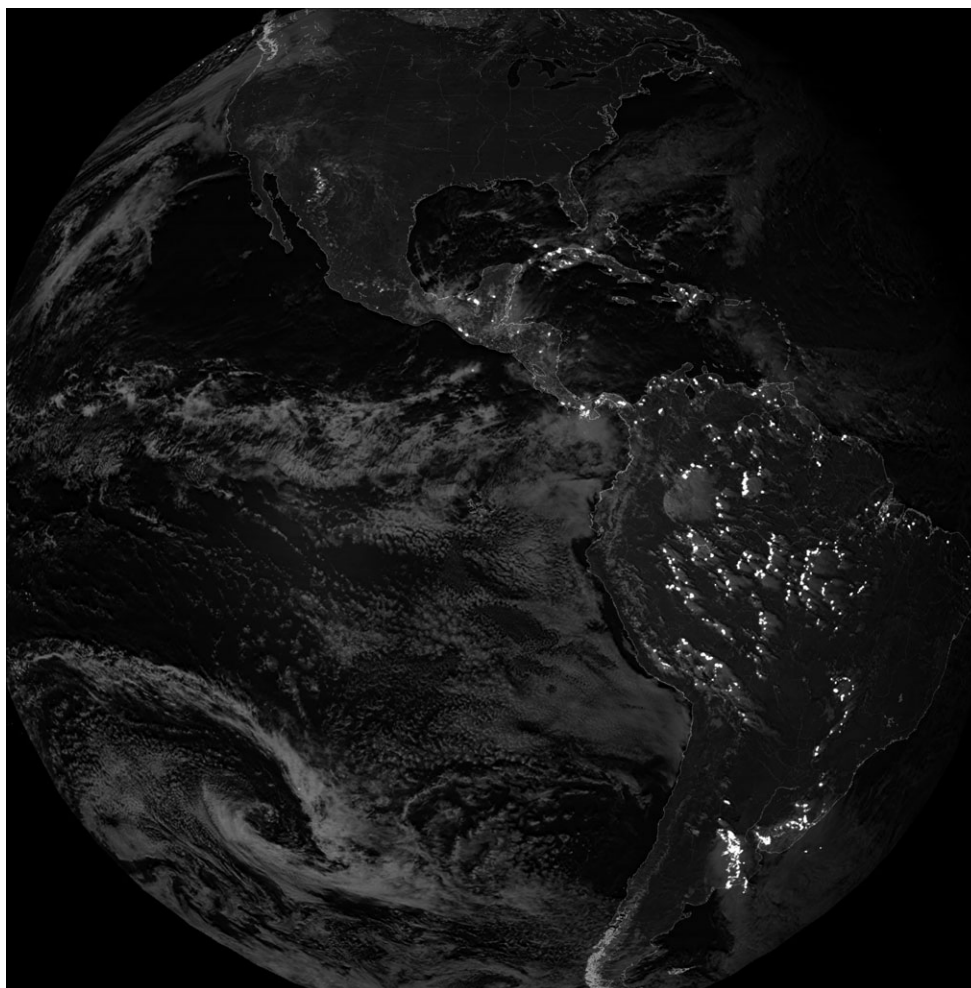


Fig. 1. Example whole-globe image from GLM, showing 20 min of accumulated lightning event detections in 600,000 frames during 20:00–20:20 UTC in the afternoon of October 18, 2017, over a mostly daytime cloud background image.

is defined as having dimensions 6394.137×6362.752 km. Example altitudes are listed in Table 2. For bolides, which appear at several times higher altitude, a significant parallax will occur.

Time tags also suffer from that parallax effect, but are less important. Every event is time-tagged on the satellite, to a precision of $\ll 1$ ms using the GPS. The origination time is computed by the ground system on the same lightning ellipsoid as the geolocation information, with the light travel time from the atmosphere to GLM being of order 60 frames (0.12–0.13 s). This origination time also takes into account the focal plane integration time and processing delay in the GLM sensor unit, such that the origination time is valid at the middle of the image integration period. Origination times can be improved once the bolide altitude is known from other sources, but will differ from those reported by <0.3 ms.

GLM event energies (expressed in Joules) are not the radiated energy released in the event, but relate to the

irradiant energy received at the aperture of the instrument. The GLM radiometric accuracy is known from laboratory measurements on the ground (Koshak et al. 2000). GLM was calibrated by using a large integrating sphere and taking images at various illumination levels to determine spectral radiance (units $\text{W}/\text{m}^2\text{-sr-nm}$) per digital number (DN) for each pixel. This provides the response of the instrument to static illumination (i.e., clouds) over the full 14-bit dynamic range.

Since lightning event detection is a transient on top of a more static background, the slope of this response was measured for 32 values of background intensity, corresponding to the five most significant bits (range 0–31) of the background intensity in that pixel (the BGMSB value, or back ground most significant bits). For each pixel, the BGMSB is measured and a lookup table is used to determine the instrument noise level, and from that the threshold level. The threshold will tend to stay constant despite the additional light of the

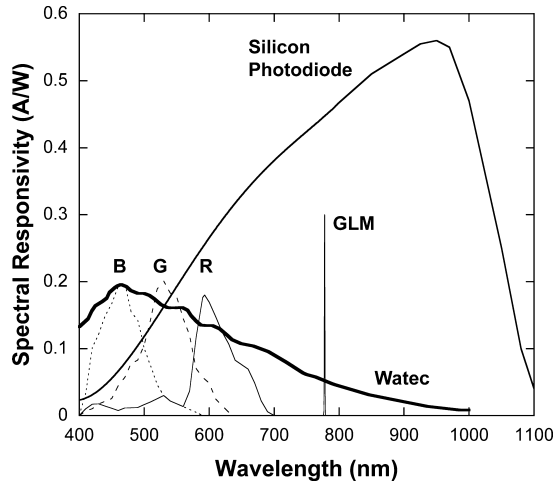


Fig. 2. Spectral responsivity of the narrow spectral pass band of GLM, compared to the typical silicon photodiode sensor material used in photometers onboard US Government satellites (from Tagliaferri et al. 1998), that of the Watec (Sony ExView HAD) low-light CMOS sensor used in the SkySentinel allsky cameras (Yang et al. 2017), and that of a Nikon D300 digital still camera’s R, G, and B color pixels, the latter based on the Quantum Efficiency QE_{λ} of Sigernes et al. (2009), expressed in ampères per watt (R_{λ}) based on: $QE_{\lambda} \sim R_{\lambda}/\lambda * (1240 \text{ W nm}^{-1} \text{ A}^{-1})$, with λ the wavelength.

bolide, because the background change is limited to ± 2 DN/frame. The BGMSB value is reported with each detected event, and used on the ground to index into a lookup table of radiometric calibration factors for each pixel, in units of energy (J) per DN.

The resulting event flux is first corrected for the cutoff of the triplet 777 nm oxygen lines by the GLM filters as a function of angle of incidence, shown schematically in Fig. 3. Three interference filters of increasingly narrow spectral width are designed to suppress stray light from the Sun, which can come just outside the field of view. The solar rejection and solar blocking filters combine with the narrow-band interference filter to determine the pass band. The angle of incidence determines the effective central wavelength and bandwidth of each filter (Goodman et al. 2013). All spectral filters are temperature controlled, ensuring that those central wavelengths remain stable. The combined GLM band pass also changes center wavelength with angle of incidence (and also slightly in band width), allowing a smaller portion of the triplet into the instrument at the edges of the field of view (Fig. 3). The correction to the flux for this cutoff amounts to $<20\%$ for incidence angles $\alpha < 7^{\circ}$ (in terms of viewing direction relative to nadir), but increases rapidly for higher incidence angles (Fig. 3). At the geostationary viewing distance, bolides are at a near-constant angle of incidence, so that this correction is a constant for the entire bolide light curve.

Table 2. Altitude of the lightning ellipsoid above the WGS 84 reference ellipsoid for GPS and the incidence angle of light on the GLM entrance aperture for 75°W longitude.

Latitude ($^{\circ}$)	Radius WGS 84 (km)	Altitude (km)	Incidence angle @ 75°W ($^{\circ}$)
0.0	6378.14	16.00	0.00
10.0	6377.49	15.70	1.77
20.0	6375.62	14.84	3.46
30.0	6372.77	13.51	4.98
40.0	6369.27	11.89	6.28
50.0	6365.56	10.15	7.31
60.0	6362.08	8.51	8.05

The measured intensity of the oxygen triplet lines is further multiplied by the integration time (which is not the same for all pixels), and by the effective bandwidth (also not the same for all pixels as it depends on angle of incidence). That result (now in $\text{J}/\text{m}^2\text{-sr}$) is multiplied by the footprint on the ground calculated separately for each pixel (m^2), and by the steradian angle (sr) given by the GLM aperture area and the altitude of the satellite. This provides the irradiant energy (adjusted to be in units of Joules) of the oxygen triplet emission lines over the entrance aperture of the GLM instrument, which is shown in various figures in this paper.

The total radiant energy emitted (E) is calculated by integrating the irradiant energies over all time intervals and all directions, making further assumptions about the distance to the event (position assumed to be at the lightning ellipsoid), and that the energy was emitted in all directions. To integrate over all directions, the GLM event energies need to be multiplied by $4\pi R^2/(\pi r^2)$, with R = the distance from the source to the GLM satellite ($\sim 35,780$ km (nadir) to $\sim 42,170$ km (edge) from the lightning ellipsoid) and r the radius of the effective aperture (\sim a factor $1.61\text{--}2.23 \times 10^{16}/0.0095$), and multiplied by the contribution of the pass band of GLM over the complete blackbody continuum curve. To enable a direct comparison with the broadband USG-sensor detections (Fig. 2), we adopt the same blackbody temperature of 6000 K (Tagliaferri et al. 1998), resulting in a correction factor of 1.018×10^3 .

The GLM on-orbit responsivity is expected to remain stable for the lifetime of the mission, but will be monitored throughout the mission, not by calibration against an internal absolute standard calibration source, but by comparing GLM background frames with images obtained by the coaligned Advanced Baseline Imager (ABI). Bright, deep convective clouds are considered Lambertian surfaces. When these are observed together with ABI, the radiometric response of GLM can be measured and trended over time (Rafal et al. 2016).

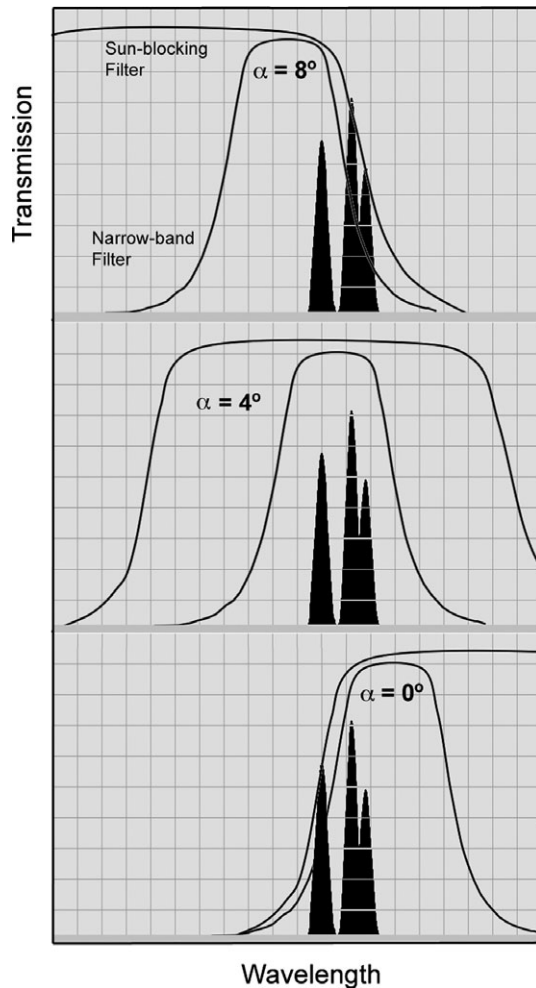


Fig. 3. Schematic illustration of how the band pass of the sun-blocking and narrow-band filters shift as a function of angle from nadir α . The signal is corrected to reflect how much of the 777 nm oxygen line triplet emission (dark) is in the pass band.

Previous studies with the GLM-like Lightning Imaging Sensor (LIS) on the NASA Tropical Rainfall Measuring Mission showed $<1\%$ change in radiometric response over 17 yr of in-orbit observations (Buechler et al. 2014).

RESULTS

Table 3 gives an incomplete list of 10 bolides and fireballs detected by other sensors in the GLM field of view during its commissioning phase from February to December 2017. Six out of seven of the USG-reported bolides were detected. One detected bolide resulted in recovered meteorites. GLM also detected at least three other less bright fireballs reported from ground-based video observations over the United States. The 0.13 kt bolide that was not detected occurred on February 22 (Table 3), when GOES-16 was still doing postlaunch

test maneuvers and was not able to transmit between about 18:00 and 19:30 UTC that day. It was initially reported to have occurred on February 21, but after GLM did not detect a bolide on that date, USG provided the correct date.

The Bright March 11, 2017 West Atlantic Bolide

The most energetic bolide detected during this period appeared over the western Atlantic on March 11, 2017 (Table 3). USG satellite data reported a yield of 2.9 kt, corresponding to a 2–3 m diameter asteroid at 30 km s^{-1} , 3–4 m at 20 km s^{-1} , or 5–6 m at 12 km s^{-1} entry speed. Such events are detected only about once per year over the whole globe (Brown et al. 2002a, 2013). The USG satellites did not provide an entry speed or velocity vector.

The GLM light curve (Fig. 4), depicting the pixel-integrated irradiant energy as a function of time, was extracted by summing the signal of all illuminated pixels in each frame that appeared to belong to the bolide. The GLM-provided intensity calibration based on the BGMSB value corresponded to $1 \text{ DN} = 5.03 \times 10^{-17} \text{ J}$. The signal was above the GLM threshold for a total of 1780 frames recorded during 4.8 s. The full duration of the bolide is recorded, with small gaps in the record only at the time of peak brightness. The observed integrated energy value ΣE_O is given in Table 4.

It is customary in meteor astronomy to express photometry in terms of absolute visual magnitudes (m_V), which is a ratio of irradiance (F). “Absolute” here means that the irradiance is normalized to a standard viewing distance of 100 km. “Visual” refers to the visual pass band (V) centered on 548 nm. In astronomy, magnitude is defined relative to the irradiance of the zero magnitude A0 type star Vega: $m_V = -2.5 \log(F_V/F_V(0))$, with an effective color temperature of 11,500 K. The adopted standard irradiance at 548 nm is $F_V(0) = 3.67 \times 10^{-11} \text{ W m}^{-2} \text{ nm}^{-1}$ (Jenniskens 2006). If the pass band is different, the magnitude will depend on the wavelength and band pass used to measure the photon energy flux, differing from m_V up to a factor of 2 between 300 and 900 nm if the meteor has an effective color temperature of only 6000 K.

From this definition, the GLM intensity calibration of $5.03 \times 10^{-17} \text{ J/DN}$ translates to a 32 DN threshold corresponding to an absolute visual magnitude of -14.2 (Table 4). This value applies only to that pixel location on the sensor under the conditions of these nighttime observations.

Due to the long duration of the meteor, the background level could have been significantly changed, but in this case the background was not adjusted. At the time, the instrument’s real-time event processors were not tuned yet and the “background hold off” setting was enabled. This setting temporarily discontinued the

Table 3. Time and location of bolides discussed in this paper (latitude, longitude, and altitude), as well as direction of motion (azimuth from north and elevation) and total radiated energy (E).

Date	Time (UTC)	Location	Lat. (+N,°)	Long. (+E,°)	Alt. (km)	Az. (N,°)	El. (°)	Yield ^a (kt)	E^a (10^{10} J)	Src.
February 06, 2017	07:25:16	Wisconsin	+43.4	-88.0	~40	~49	~23	~0.010	—	IS, S
February 22, 2017	18:47:30	Argentina	-50.7	-66.0	—	—	—	0.13	3.8	USG
March 11, 2017	04:51:21	W. Atlantic	+28.3	-60.2	28.0	—	—	2.9	126	USG
May 26, 2017	05:39:00	Lufkin, TX	+31.9	-91.7	~30	~104	~41	—	—	S
July 23, 2017	06:12:38	Brazil	-6.6	-69.7	38.0	350	22	0.12	3.5	USG
July 31, 2017	22:01:35	Baja Calif.	+24.7	-118.5	—	—	—	0.19	5.8	USG
September 05, 2017	05:11:27	British Col.	+49.3	-116.9	36.0	280	13	0.13	3.8	USG
October 09, 2017	12:51:48	Bolivia	-18.3	-64.1	—	—	—	0.10	3.0	USG
November 15, 2017	03:26:46	Arizona	+34.4	-111.5	33	167	45	—	—	C, S
December 29, 2017	12:47:31	Atlantic	+14.6	-49.5	38.0	—	—	0.33	11.0	USG

^aThe impact energy of the event in kilotons of TNT computed from an empirical expression relating radiated and impact energy (Yield) and the approximate total radiated energy in the atmosphere in Joules (E); Src: USG = U.S. government satellite network, C = LO-CAMS, IS = Infrasound, S = SkySentinel.

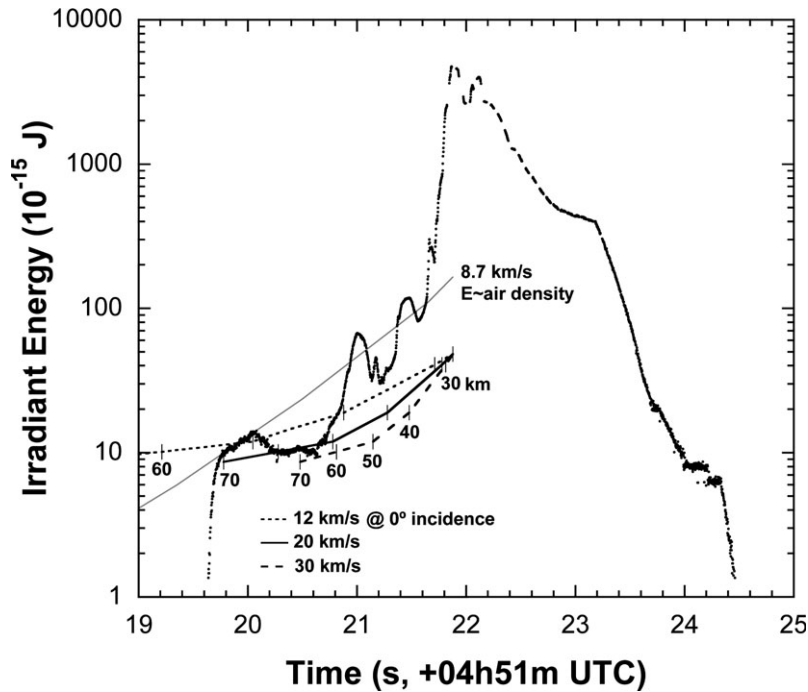


Fig. 4. The March 11, 2017 West Atlantic fireball light curve derived from GLM Level 0 data. Peak brightness is at an altitude of ~28 km. The Discussion section in this paper explains the model curves, showing the computed O I, bound/free and free/free emission for a 2 m diameter spherical meteoroid moving at 12, 20, and 30 km s⁻¹ for a zenith angle of 0°. Vertical dashes on each curve are altitude markers. In contrast, the solid gray line shows the expected variation if the luminosity is proportional to the air density at that altitude, instead, and the vertical component of the entry speed is 8.7 km s⁻¹.

background averaging process upon detection of an event. Because the scene background changes over longer time scale, this light curve is unaffected by background.

The later part of the light curve shows small gaps (between 21.8 and 23.0 s, Fig. 4). These are caused by first-in first-out (FIFO) overflows, when one component in the data flow has not been able to read all the data coming from an upstream component. The queues that

accumulate events for each section of the focal plane are 1024 deep, and are cleared out every 32 frames. If more than 1024 events occur in one section in 32 frames, the FIFO fills up and additional events are dropped. Since the video stream is processed (in this case) from the eastern edge of the image toward the center of the image, all the events are listed from right to left (currently east to west) in order of pixel

Table 4. Parameters derived from GLM detections, including projected geolocation of peak brightness, the projected direction of motion (azimuth relative to north), altitude of the projection surface: the lightning ellipsoid altitude (LEA), the viewing angle from nadir (α), the light curve threshold of absolute visual magnitude (ground-based and GLM combined), the light curve-integrated (Σ) irradiant energy (E_O) and corrected for parts of the light curve that were not detected based on ground-based observations and gaps in the GLM light curve (E_T), and the total radiated energy assuming continuum emission dominating over O I line emission (E).

Date	Lat. ^a (+N,°)	Long. ^a (+E,°)	Az. ^a (N,°)	LEA (km)	α (°)	> <i>mv</i> (magn.)	ΣE_O (J)	ΣE_T (J)	E (10^{10} J)
February 06, 2017	+44.1	-87.8	^b	11.3	6.8	-4.0	4.6e-13	1.3e-12	0.081
February 22, 2017	N.D. ^c	N.D.	N.D.	6.9	7.4	N.D.	N.D.	N.D.	N.D.
March 11, 2017	+28.2	-61.8	240	13.8	5.2	-14.2	6.9e-10	1.2e-9	260
May 26, 2017	+31.8	-95.2	120	13.2	5.7	-4.0	3.1e-13	6.1e-13	0.011
July 23, 2017	-6.8	-69.4	140	15.8	1.5	-13.4	1.7e-11	1.9e-11	3.4
July 31, 2017	+24.7	-118.4	137	14.2	7.2	-14.2	4.6e-11	4.7e-11	7.4
September 05, 2017	+49.9	-117.2	108	10.2	8.1	-2.0	7.1e-11	8.4e-11	8.7
October 09, 2017	-18.7	-64.2	331	14.8	3.7	-14.0	2.3e-11	2.5e-11	4.9
November 15, 2017	+34.3	-111.6	^b	12.8	7.2	+4.3	1.1e-13	3.0e-13	0.018
December 29, 2017	+14.6	-49.4	293	15.4	4.9	-13.5	7.4e-11	8.9e-11	19.1

^aAs seen projected onto lightning ellipsoid.

^bSingle-pixel detection with no azimuth information.

^cNot detected due to data dropout.

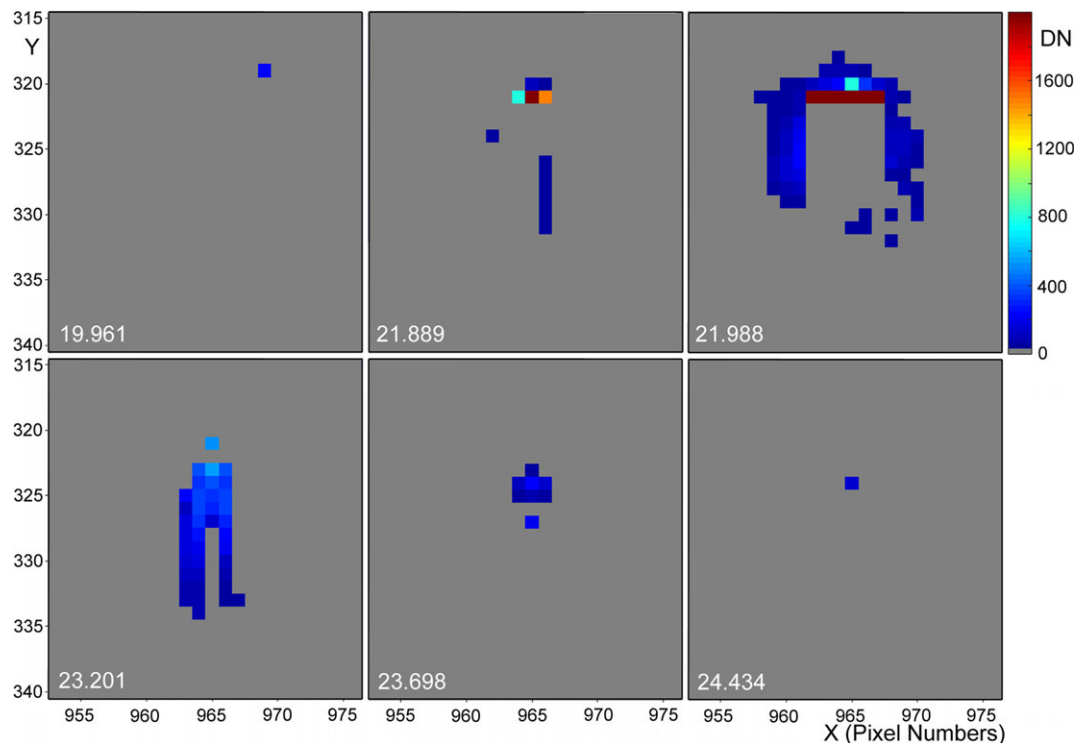


Fig. 5. Raw, unprocessed GLM Level 0, data pixels of the West Atlantic bolide. Each cropped frame is labeled with time in seconds (+04h51m UTC). X and Y axis are given in pixel coordinates, while the color scale is proportional to digital number (DN) intensity.

identification number until the FIFO fills up. There will be no more events to the left after that, nor any in subsequent frames until the 32-frame scan sequence is complete and the FIFO is emptied. This phenomenon relates only to the number of detected events, not to the

saturation of the image. The final record at the end of each sequence is incomplete and was removed. The gaps may hide brief flares, but typically last <20 frames.

This event was also bright enough that both electronic saturation, blooming, and optical distortions

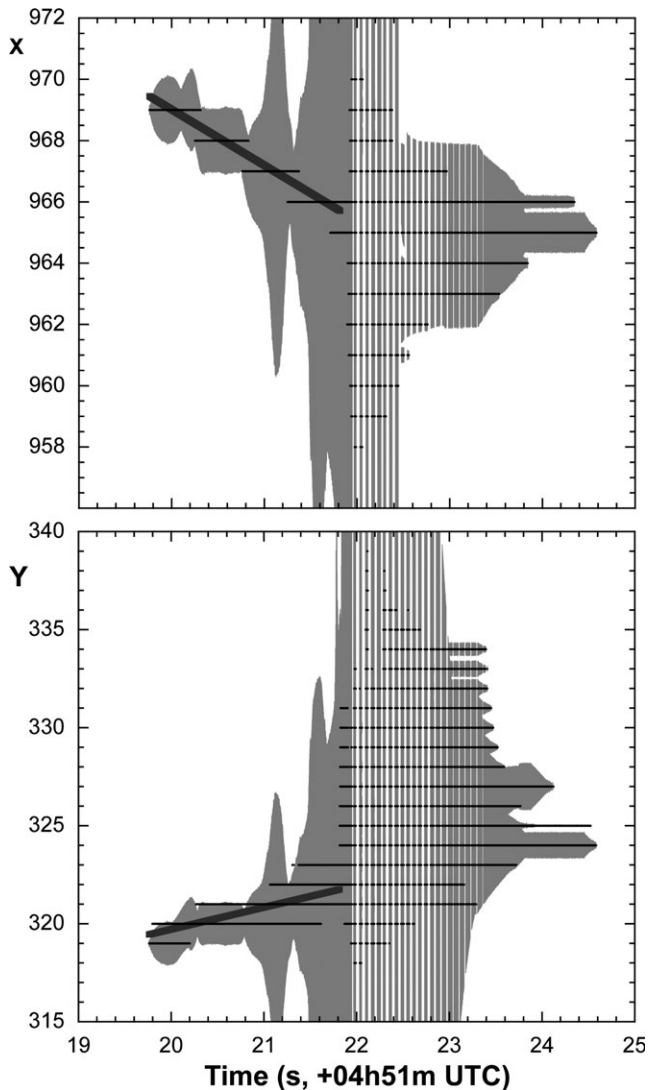


Fig. 6. The March 11, 2017 West Atlantic fireball motion as seen in the X and Y position of threshold events (a black dot for each frame, making solid black lines). Vertical gray lines from each dot are proportional to the brightness of that threshold event. A thick line depicts the motion of the meteoroid itself.

occurred. These effects are more evident in an animation of the subarea of the focal plane (Fig. 5). The bolide briefly saturated the GLM sensor during about 20 frames, when the intensity reached its maximum value of 2^{14} DN. CCD blooming spills electrons into neighboring pixels when the bolide becomes too bright (at 21.988 s, Fig. 5). In addition, the bolide illuminates the clouds or the ocean surface below at the time of peak brightness. Threshold events occur over a large circular area, but displaced from the saturated pixels due to projection (the bolide being high in the atmosphere and seen under an angle against the ocean surface). A number of weakly illuminated pixels below the brightest pixels are

suppressed (no threshold crossers) due to undershoot in the analog readout, only slightly lowering the total measured intensity at this time. Finally, time stamps 21.889 and 23.201 show long streaks below what were formerly the brightest pixels. Such persistent *rebound false events* occurred due to the experimental configuration of the real-time event processor (RTEP) on that particular date, when the instrument was still being adjusted.

A projected northeast to southwest motion of the meteor is evident early in flight, but more difficult to see later on when the signal overlaps that of persistent emission (Fig. 6). The object strongly decelerated or fully disintegrated following the main eruption. The meteor was first detected in pixel $X = 969.45$, $Y = 319.45$ at 19.762 s UTC and just before the main eruption was at $X = 965.71$, $Y = 321.76$ at 21.817 s UTC, moving in projection against the globe over 4.3 pixels in 2.055 s.

The Bright December 29, 2017 Atlantic Bolide

USG satellites recorded a 0.33 kt bolide with a total radiated energy of 11.0×10^{10} J over the Atlantic Ocean well off the coast of French Guiana and Suriname on December 29 (Table 3). Peak brightness occurred at a relatively high 38 km, but no speed or direction of motion was obtained.

This is the second most intense bolide detected in the GLM field of view during this period with a signal duration of 2.6 s (Fig. 7). The bolide occurred during daytime, so different pixels have a different amount of background light (a.k.a. the cloud scene), which caused the onboard detection thresholds to range between 32 and 43 DN, autonomously selected as needed to accommodate background scene photon noise. In this case, no more than 4 pixels exceeded the threshold level in each frame. The bolide did not fill the event FIFOs, so there are no disruptions in the data. Only a few frames did saturate in 1 or 2 pixels. The calibration ranged 2.52 – 2.98×10^{-17} J/DN for the various pixels, or about -13.5 absolute visual magnitude at 32 DN (Table 4).

Level 0 data positions are geolocated to the center of each pixel. In Level 2 data, event groups are defined that provide more accurate pixel-averaged locations of the meteor. The geolocated Level 2 data clearly show motion of the meteor (Figs. 8a and 8b), which ceases to be linear as a function of time following the main flares, suggesting after the flares there were a number of strongly decelerating (small) fragments.

Figure 8c shows the position of Level 2 event groups, grayscale coded by the sum pixel intensity. Groups with one event alias to the center of the GLM pixel (light gray). Groups with two events alias to the rectangular pixel grid, along the line that connects the center of the GLM pixels (dark gray). Groups with

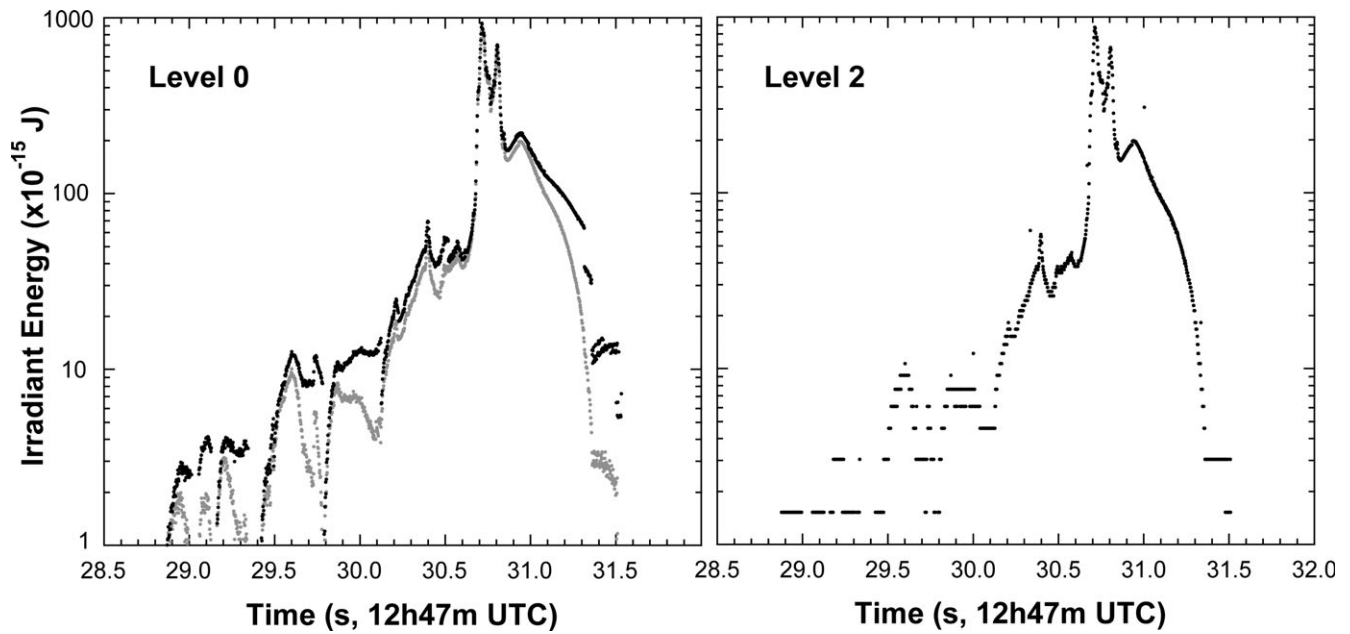


Fig. 7. The December 29, 2017 Atlantic Ocean fireball as detected in GLM Level 0 (left) and Level 2 data (right). Level 0 data are shown both with (dark) and without (gray) background correction. Peak brightness is at an altitude of ~ 38 km.

three or more events are the ones that provide a better subpixel geolocation accuracy (black).

The reported brightness is affected by the onboard automated adjustment of the background level. The background change in each pixel is defined as $1/64$ th of the intensity level of the current frame added to $63/64$ th of the previous background average, before applying a maximum 2 DN/frame limit to the change. If the intensity change is sufficiently large, at least four times the threshold level (~ 130 DN), then the rate of change hits this 2 DN/frame limit.

For the brightest pixels (Fig. 8c), this provides a recipe to fully correct the background drift. Although the background intensity level in each pixel is reported only in steps of 512 (five most significant bits of a 14-bit signal, the BGMSB value), it can be reconstructed to higher precision because the expected slope of 2 DN/frame matches the change in the reported background. The correction is straightforward and the result is shown together with the uncorrected profile in Fig. 9. The three brightest pixels had a background of 2432 ± 30 DN (for $X, Y = 981, 493$), 1536 ± 30 DN (for $X, Y = 981, 492$), and 3304 ± 30 DN (for $X, Y = 980, 493$), respectively. For bright pixels such as these, the influence of this background change is small. Bright pixels contribute most to the total detected energy, and as a consequence background drift has little impact on the calculation of the total radiated energy of the bolide.

The background drift is more important for the early weak part of the light curve. Note how the early oscillations in brightness in Fig. 7 correlate with the

position of the meteor on the pixel. Here, the change in the background level can be reconstructed based on the measured intensity in each frame provided that there is an unbroken chain of consecutive events in the same pixel. In this case, we find some pixels with small time gaps (\sim ms long), especially toward the end of each sequence.

While the intensity stays below the threshold (~ 32 DN), the change in cloud scene background remains undetermined, but is $< \pm 0.5$ DN/frame. Pre-exposure by the meteor also stays below 0.5 DN/frame, but can accumulate if the meteor moves slowly from pixel to pixel. The meteor moves at a known pace across the pixels and the effect of pre-exposure can be calculated if the point spread function of the meteor is known. This, we did not attempt to do here. Finally, after the signal decays and the background catches up with the signal, the background change is again undetermined. At that time, persistent emissions will also affect the brightness.

This background correction requires the detail present in Level 0 data. The Level 2 data suffer from loss of least significant digit information, being digitized in steps of 30 DN. As a result, much detail at earlier parts of the light curve is lost (Fig. 7, right panel). The quantization is introduced at the L1b/L2 interface, since the upstream L1b product encodes energy as double-precision floating point, retaining the full energy resolution of the instrument. Only in L2 is this encoded as int16 with a scale factor of 1.526×10^{-15} J (30 DN), with attendant loss of the numerical precision by not capturing the least significant bits of the event intensity (see netCDF file metadata). Note that there is no loss of

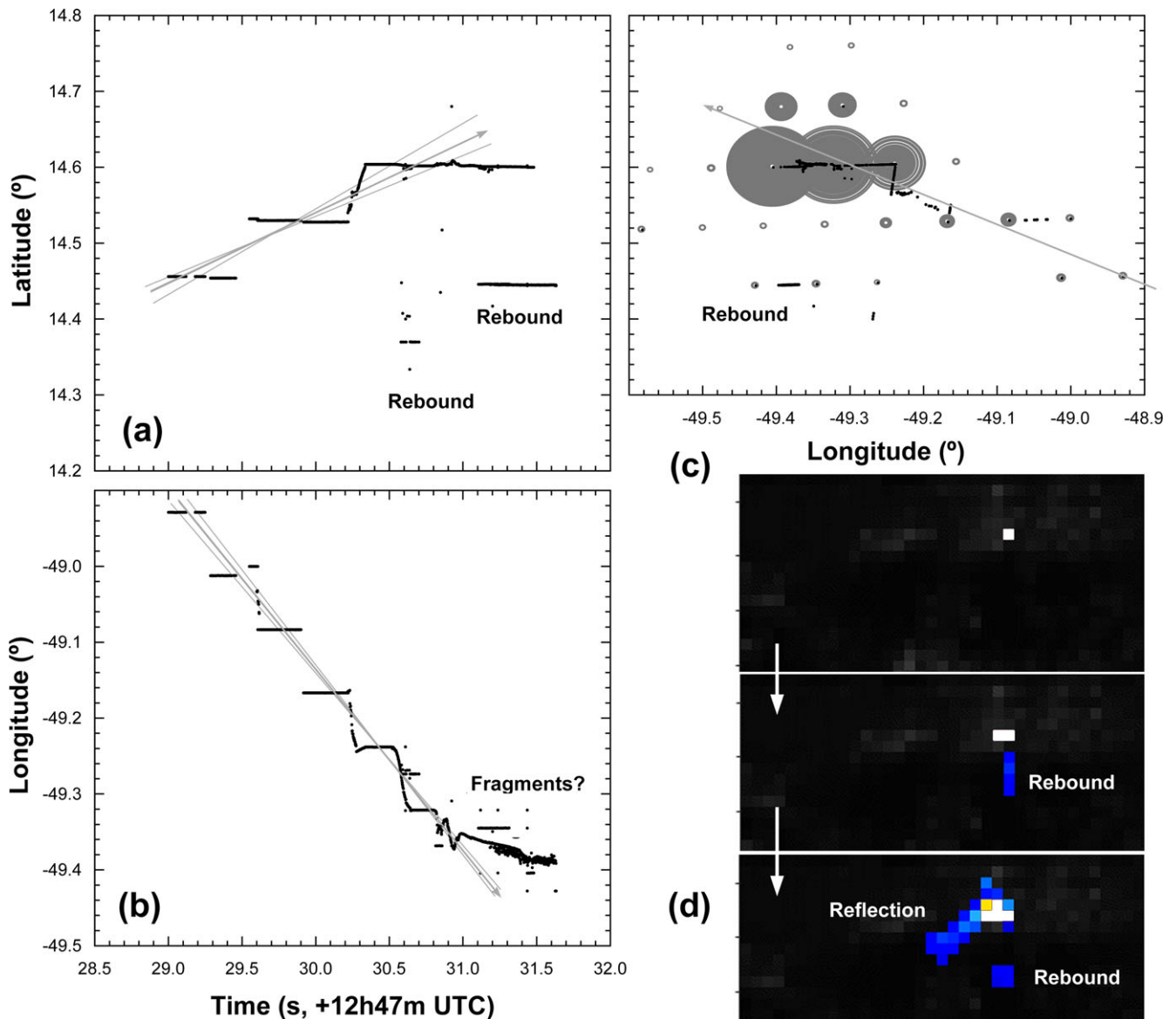


Fig. 8. Level 2 geolocation of threshold event groups for the December 29, 2017 Atlantic Ocean bolide. a) Latitude as a function of time, with gray lines showing the likely direction of bolide motion. b) Longitude as a function of time. c) Latitude (same scale as [a]) versus longitude of threshold crossovers, with gray circles marking the brightness of each pixel. d) Three cropped frames that show the position of rebound and reflection signals relative to the moving meteor. (Color figure can be viewed at wileyonlinelibrary.com.)

sensitivity from this quantization. The instrument still detects the least significant threshold crossovers and the ground system still reports all of it, albeit with lower energy resolution in the resulting light curve.

In addition, the ground-based Level 1b filter processing discarded a significant number of “nonlightning” events that are not present in the Level 2 data product. This bolide generated 3427 raw Level 0 events, 384 were removed by the second-level threshold filter, 265 by the overshoot filter, 119 removed by the radiation track filter, 63 were removed by failing the coherency test, 12 by coherency timeout, 8 by the

contrast leakage filter, and leaving 2576 events identified as “lightning.” However, the remaining events contain 99.5% of the original signal. Note occasional quantization errors in the time tags reported in Level 2 data cause points to be twice the adjacent values in the light curve at 30.124, 30.458, 31.126, and 31.458 s UTC, an issue that remains to be resolved.

Some of the remaining threshold events occurred south of the meteor (Fig. 8c), accounting for 16% of the signal. These are rebound events. The reflection of a bolide’s light from the ground will always fall near the

bolide on a line between the bolide and the subsatellite point, and there is such a reflection in this case (Fig. 8d, lower panel). The relative position of the reflection can perhaps be used to derive the altitude of the bolide. Rebound events, on the other hand, will occur in undershot pixels that are subsequently read to a pixel that was recently strongly illuminated by the bolide, roughly southward in the northern hemisphere as is the case here, or northward in the southern hemisphere. The main distinction between rebound events and optical reflection events is in the time domain. A reflection occurs simultaneously with the larger signal. Rebound occurs with a delay, after a larger signal creates undershoot that is sustained enough to get baked into the background average. Rebound signals should not be included in the light curve.

After calculating the cumulative background changes from Level 0 data, the corrected light curve is shown with dark symbols in the left graph of Fig. 7. There remains an initial rapid rise of intensity in each pixel, which may be due to background change induced by pre-exposure before becoming bright enough to meet the threshold level. After taking that into account, a smooth increase in brightness is observed, with some remaining irregularity that may well be intrinsic.

The light curve of this bolide has much structure to it, with at least eight narrow flares superimposed on the main double-peaked eruption alone. Combined with the high altitude of peak brightness, this implies a weak, brittle material. The main disruption occurred at 12:47:30.713 UTC, during which the number of event pixels dramatically increased to 18. The pixel number profile (data not shown) is almost symmetric relative to the peak time. The (unsaturated and less bright) flare following the main disruption did not cause such blooming.

The July 31, 2017 Bolide Off Baja California

The third brightest bolide known to have been recorded during this period is the USG-detected bolide off the coast of Baja California, which provided no altitude or velocity vector information (Table 3). Potential visual observers in Mexico did not report to the American Meteor Society's fireball reporting web page.

In GLM data (Fig. 10), the meteor moved 3 pixels in a NNE direction. The beginning part did not change in brightness in a continuous manner, but appeared to be composed of a number of brief flares. No pixels were saturated, but again the number of threshold crossings around the main object changed over time. The calibration corresponded to a 32 DN threshold absolute visual magnitude of -14.2 (Table 4).

The detection may represent a phase of the bolide light curve when the meteoroid has penetrated deep into Earth's

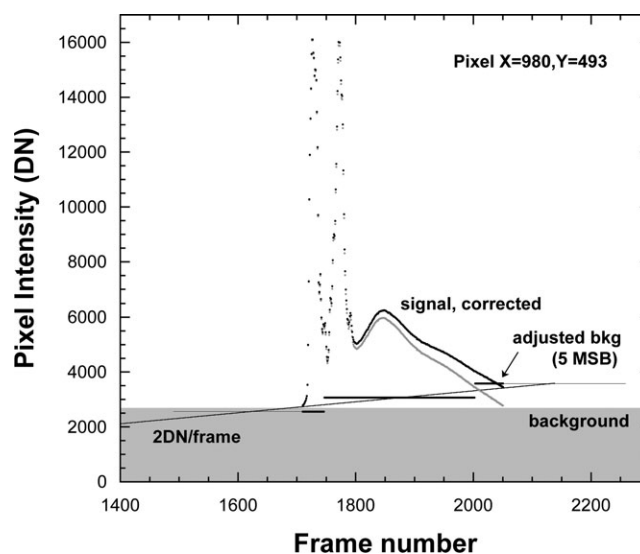


Fig. 9. Intensity variation for a single bright pixel of the December 29, 2017 Atlantic Ocean bolide. Gray points show the reported intensity and black points the intensity corrected to a constant pre-event background level (gray area). The thick gray line has a slope of 2 DN/frame and is matched to the point half way between steps in the five most significant bit values of the reported background intensity level (black lines).

atmosphere, just before the main disruption. The light curve has the same rounded eruptions of brightness seen in the West Atlantic bolide, but the number of events over time is markedly different (shown in Fig. 10). The second peak has at its onset a sharp multiplication of events, suggesting it briefly brightened the surroundings, the first peak does not. The brightened surroundings could point to flares too brief to be resolved even by GLM, a potentially important diagnostic of fragmentation.

The British Columbia H6 Meteorite Fall of September 5, 2017

A meteorite fell on September 5, 2017 near the town of Crawford Bay in British Columbia, Canada (Hildebrand, personal communication). USG sensors determined it to be a relatively small 0.13 kt bolide (Table 3). The bolide was reported by 314 visual observers (AMS fireball 3068-2017) and recorded in ground-based video cameras, from which broadband photometric data were extracted to compare to the narrow-band GLM data. The positions of discrete fragmentations that produced flares, as derived from the triangulated trajectory, are summarized in Table 5. Based on the triangulated trajectory, the meteor moved at $\sim 16.2 \text{ km s}^{-1}$ before fragmentation. Meteor fragments were visible at least as low as 18.9 km altitude.

Figure 11 shows the light curve derived from the sum pixel intensities, now expressed in absolute visual

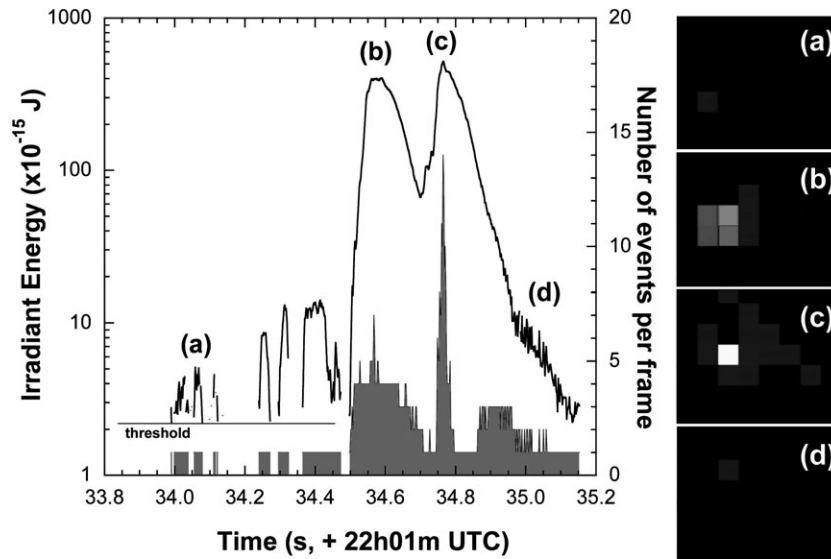


Fig. 10. The July 31, 2017 bolide off Baja California. The light curve is plotted together with a histogram of the number of events in each frame. The sidebar shows four frames, with shades marking the intensity of each pixel, in arbitrary units, the sum of which adds up to the reported irradiant energy in the graph.

Table 5. The position and altitude of fragmentation events detected in British Columbia meteor (event number labels in Fig. 11), with a combined uncertainty of ~ 1 km in latitude and longitude and ~ 0.3 km in altitude. GLM origin time and Summit video recorded times are relative to 05h11m00s UTC. COTR video channel two times are relative to the start of frame capture.

GLM event #	GLM time (s)	GLM intensity (DN)	Summit time (s)	COTR time (s)	Lat. (+N, $^{\circ}$)	Long. (+E, $^{\circ}$)	Alt. (km)
b-1	26.856	370 ^a	26.804	8.867	49.5772	-116.8327	35.46
b-2	27.909	1100 ^a	"	-	-	-	-
b-3	27.963	1800 ^a	"	-	-	-	-
b-4	27.005	2700 ^a	"	-	-	-	-
b-5	27.034	3320	26.983	9.034	49.5938	-116.8338	34.09
b-6	27.058	3100 ^a	"	-	-	-	-
b-7	27.183	1300 ^a	"	-	-	-	-
b-8	27.229	1100	"	-	-	-	-
b-9	27.285	590	"	-	-	-	-
c-1	27.332	1380 ^a	-	-	-	-	-
c-2	27.359	2430	-	-	-	-	-
c-3	27.368	2480	27.325	9.334	49.6248	-116.8358	31.54
d	27.660	205	27.636	9.634	49.6592	-116.8380	28.72
-	-	-	27.891	9.935	49.6853	-116.8398	26.58
e-1	(28.146)	140 ^b	-	-	-	-	-
e-2	28.242	75	28.213	10.235	49.7114	-116.8415	24.44
e-3	28.266	75	"	-	-	-	-
e-4	28.309	56	28.266	-	-	-	-
e-5	28.313	52	"	-	-	-	-
e-6	28.338	47	"	-	-	-	-

^aWeak bump on slope.

^bIsolated single frame.

magnitudes, and is normalized to the apparent visual magnitude of the Moon. Moon and meteor images bloom in a similar way and no saturation corrections were applied. The Moon was in waxing gibbous phase

with 99% of its visible disk illuminated, corresponding to an apparent visual magnitude $m_V = -12.6$. The Moon is nearly a continuum source with a spectrum similar to that of sunlight (\sim blackbody with $T = 5778$ K).

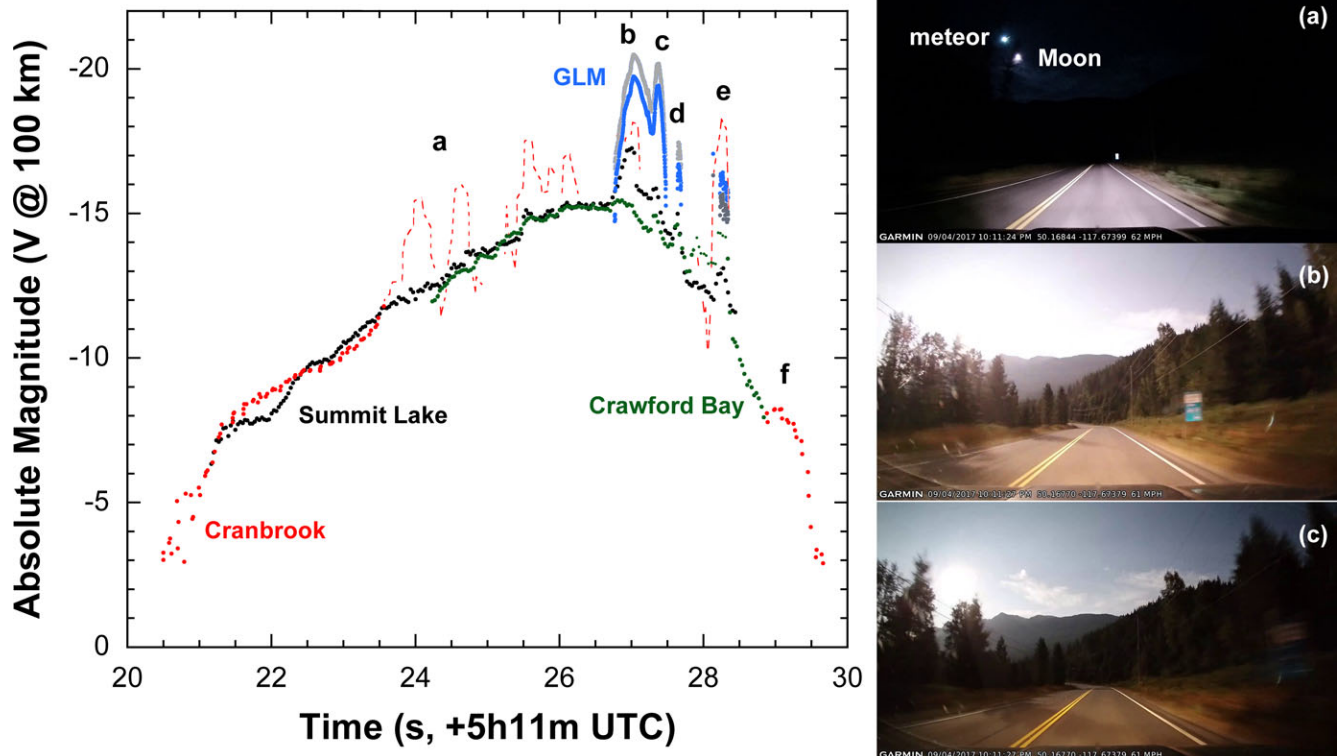


Fig. 11. The September 5, 2017 British Columbia bolide with peak brightness at 34.1 km. The GLM-derived results (gray: as reported; blue: without O I line correction applied) are compared to ground-based video observations of the bolide, depicted in terms of visual magnitudes, with flare event groups labeled with letters. Images to the right show Summit Lake video at (a) 5h11m24.12s, (b) 5h11m27.29s, and (c) 5h11m28.02s UTC (time corrected to GLM).

A dash cam video equipped with a GPS receiver detected the meteor from a moving car traveling near Summit Lake (50.16794°N , $117.67386^{\circ}\text{W}$, $+772\text{ m}$) northwest of the meteor by $\sim 182\text{ km}$ (start) to $\sim 78\text{ km}$ (end). The meteor appears in cloudless parts of the sky, with brief obscurations by foreground trees near its end. The Moon is visible in the video close to the path of the meteor and near the point where the meteor reaches a comparable magnitude. Moon and meteor are identically bright in only one frame (Fig. 11a). Many forest fires were burning in southern B.C. at this time; some smoke is visible in the brighter portions of the video, but it was not as thick as at other nearby video locations. Visibility seems good when the meteor lights up the landscape (Figs. 11b and 11c).

At the same time, a video security camera operated in Crawford Bay (49.688°N , 116.818°W , $+600\text{ m}$) showed a backyard indirectly illuminated by the Moon and later by the bolide, which passed almost overhead (Fig. 11, green dots). The moment when the meteor's light became apparent was taken as it having reached the Moon's brightness. The meteor itself is not detected. The illumination from both the meteor and the Moon would have been altered by smoke from forest fires,

with the nearest fire only $\sim 22\text{ km}$ to the southwest, and possibly differently so with changing elevation of the meteor. The elevation of the meteor increased from $\sim 65^{\circ}$ to $\sim 87^{\circ}$ during the perceptible illumination. We have not attempted a correction for this.

The meteor was also captured by Node 28 of the Spalding (SkySentinel) Allsky Camera Network (<http://www.goskysentinel.com/>) at the College of the Rockies (COTR) at Cranbrook at 49.52°N , 115.74°W , $+937\text{ m}$, $\sim 140\text{--}88\text{ km}$ from the meteor. A 640×480 pixel Wattec Wat902H2 Ultimate camera with 4 mm allsky lens recorded video frames at a rate of 25 frames per second (PAL). The Moon is in the scene, but away from the meteor. Forest fire smoke was also present at this location. This camera has a nonlinear behavior due to blooming when exceeding a certain intensity level, as a result of which small flares are more dramatically displayed than in the Summit Lake camera (red dashed lines in Fig. 11).

GLM detected the four main flares at times in good agreement with the GPS-derived times from Summit Lake (black line in Fig. 11, video-derived time corrected by $+0.13\text{ s}$). The relative peak intensities are slightly different. In particular, peak (c) is weaker in the video observations.

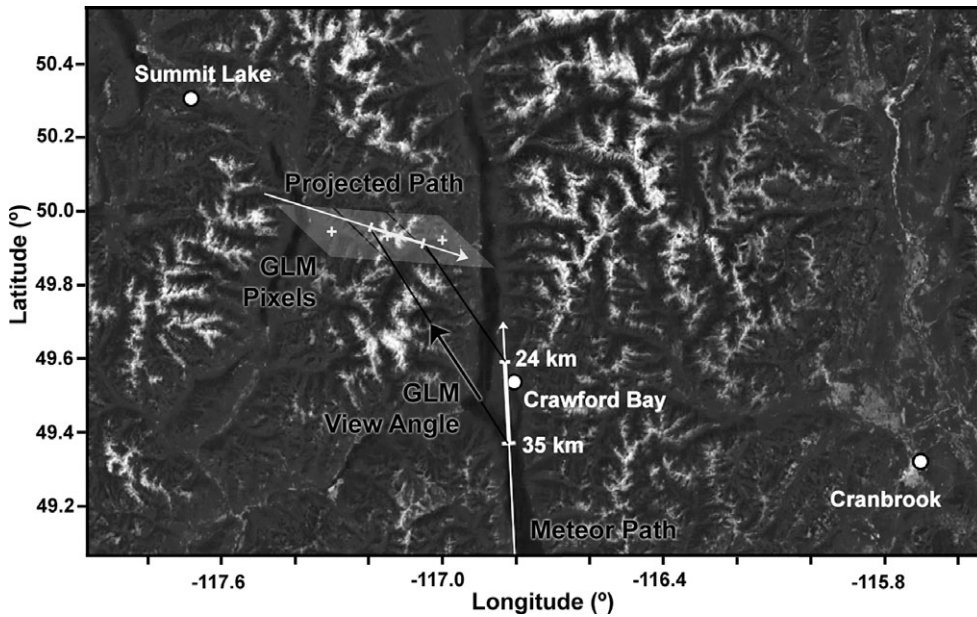


Fig. 12. The September 5, 2017 British Columbia video-derived meteor trajectory projected on the Earth surface (center), and projected on the lightning ellipsoid as seen from GLM.

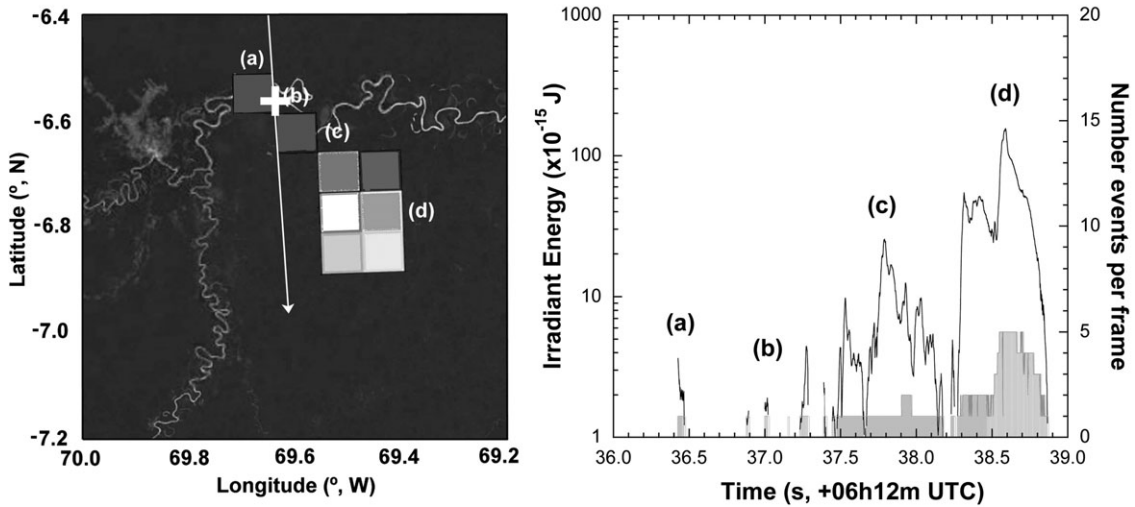


Fig. 13. The USG-detected July 23, 2017 bolide over Brazil. Left: The GLM pixels and the USG-reported position (at ~38 km altitude) and meteor direction projected onto the lightning ellipsoid. Right: Light curve from Level 0 data, with alphabetic symbols marking the meteor’s pixel positions in the left picture.

The single GLM threshold event e-1 (Table 5) has no counterpart in the ground-based observations.

Figure 11 displays the GLM intensities assuming all emission is due to continuum radiation. Following Tagliaferri et al. (1998) by assuming all observed energy in the 777.4 nm wide band at the telescope aperture (E) is continuum emission from 6000 K radiation:

$$m_v = -2.5 \times 10 \log(E/(\Delta A \Delta \lambda) \times (R/R_o)^2 \times \lambda_{548}/\lambda_{777}/F_v(0)) \quad (1)$$

with Δt the exposure time 0.00199 s, A the effective lens aperture = πr^2 with r the radius of the lens aperture (0.0558 m), $\Delta \lambda$ the effective wavelength interval ($\Delta \lambda = 1.0$ nm), R the distance from GLM to the source in km, R_o the standard distance of 100 km, and $\lambda_{548}/\lambda_{777} = 1.458$, the ratio of light between 548 and 777.4 nm for a 6000 K blackbody.

The calculated intensities are about a factor of three higher than found from ground-based video data (gray curve in Fig. 11). The difference is mainly on account of the correction made for the band pass not covering the

oxygen triplet completely (Fig. 3). The B.C. meteor has the highest GLM nadir angle ($\alpha = 8.1^\circ$) of all observed meteors reported here, well outside the relatively unaffected zone of $\alpha < 7.0^\circ$. The applied correction factor was ~ 0.50 . Indeed, if the emission is dominated by continuum emission instead of the O I line triplet, then this factor should be removed, lowering the GLM intensities by a factor of two, or 0.8 magnitudes (blue line in Fig. 11). The GLM light curve starts at such low intensity value that we can exclude a larger change, or otherwise GLM should have detected the bolide much earlier. The remaining difference between GLM and ground-based observations is likely on account of saturation in the ground-based video observations.

Equation 1 can also be used to determine the GLM detection threshold. Intensity calibration values (when plotting pixel intensity versus energy) range from 1.28 to 1.61×10^{-16} J per DN. The threshold level of 32 DN would correspond to an absolute visual magnitude of -15.3 . None of the GLM pixels are saturated. At no time were more than 3 pixels associated with the meteor. The first flare had an onset that briefly illuminated 3 pixels and was of relatively long duration. The second peak did not, with all intensity contained in one pixel and of brief duration.

GLM data can also be evaluated against the ground-based triangulation of the meteor trajectory (Fig. 12). GLM observed the meteor to move over 3 pixels from 49.943°N , 117.301°W to 49.921°N , 117.001°W in projection against the tropopause lightning ellipsoid (at 10.15 km altitude, Table 2). The coordinates cluster at the center of each pixel, so that the actual meteor position in projection against the lightning ellipsoid at any given time has an uncertainty of about ± 4 km. From the position of the middle pixel, the GOES-R satellite was at an azimuth of 146.095° and elevation of 27.102° . Figure 12 shows the triangulated meteor trajectory projected against the lightning ellipsoid from this perspective. In good agreement, the video-derived trajectory falls in projection on the approximate GLM pixels.

Other USG-Detected Bolides

Two other bolides detected by USG sensors in the GLM field of view during this timeframe show light curves with a series of flares, each having a rapid onset. This behavior is similar to that of the well-documented Novato L6 ordinary chondrite fragmentation (Jenniskens et al. 2014), a strong material, where each flare resulted in the release of a number of fragments.

July 23, 2017: Brazil

The USG-detected bolide of July 23, 2017, appeared near Eirunepé over the Amazon in western

Brazil. Perhaps due to the remote location or bad local weather, no reports were submitted to the American Meteor Society. USG data put the peak brightness at an altitude of 38.0 km and show the meteor moved at that time with a speed of 17.2 km s^{-1} from azimuth = 350.4° and elevation 22.4° , with radiant coordinates at RA = 307.0° , Dec. = $+59.5^\circ$ (J2000).

GLM detected the bolide for 2.5 s, during which there was significant motion over the detector array. The motion is plotted against the lightning ellipsoid at 15.87 km above WGS 84 (Fig. 13). The direction of motion is rotated by $\sim 36^\circ$ azimuth further east from that reported from USG satellite observations. Also, the geographic position of peak brightness is about 0.14° further southeast from the position reported from USG satellites. Such large differences in position and direction were earlier noticed for the British Columbia meteor. The GLM light curve has in common with the Baja California case that the final disruption is preceded by a broad emission that did not have the sharp flaring up of the number of pixels.

October 9, 2017: Bolivia

The USG-detected bolide over Bolivia on October 9 provides no entry speed or vector, nor an altitude, suggesting it was only detected from one USG satellite. The bolide was not reported on social media to our knowledge.

GLM detected this bolide around the time it started to break apart. The light curve is shown in Fig. 14. In this case, the meteor light curve is particularly irregular. Three large flares are detected, each of which have a rapid brightness increases and a more gradual decay.

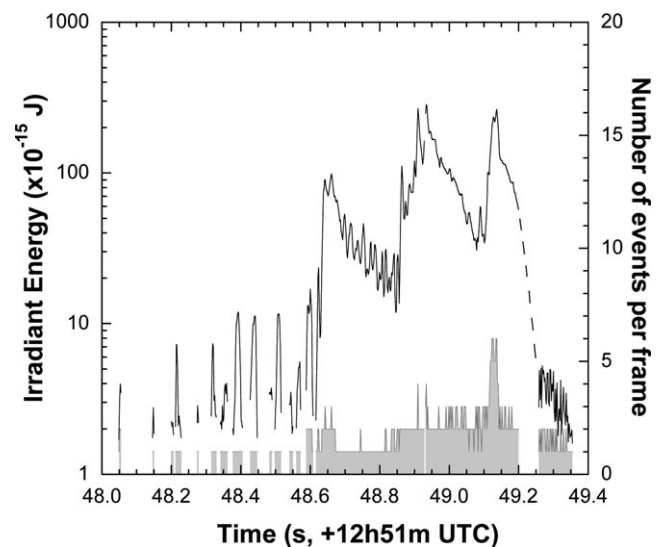


Fig. 14. GLM light curve of the USG-detected October 9, 2017 bolide over Bolivia (Level 2 data).

Only the final flare shows the rapid spreading of the image associated with the meteor.

Smaller Fireballs Near the Detection Limit

In order to see how faint a meteor would be detected, we searched for several meteors that were noticed by visual observers and recorded by video cameras of the SkySentinel network. Three fireballs (lesser bolides) were detected: in Wisconsin on February 6, 2017; near Lufkin, Texas, on May 26; and in central Arizona on November 15 (Table 3).

February 06, 2017: Wisconsin

The Wisconsin fireball was seen by at least 511 visual observers, who submitted accounts to the American Meteor Society (fireball 454-2017). Seventy-four observers reported delayed sounds from a modest airburst. An infrasound station in Manitoba, about 600 miles away, puts the lower limit impact energy at about 10 tons of TNT. This would correspond to a meteoroid about 300 kg and 60 cm in diameter (Clark 2017). Doppler weather radar detected the falling meteorites (Fries et al. 2016). Sadly, the radar signature (43.88°N, 87.55°W) was over Lake Michigan and no meteorites could be recovered.

The American Meteor Society posted several videos of the fireball, showing both direct imaging of the meteor as well as of the reflected light off a snow-lit landscape at Marshall, Wisconsin (Fig. 15). The two

most intense flares occurred toward the end, which left compact clouds of (orange colored) persistent emission that faded after about 0.26 s. The SkySentinel node 38 (Fitchburg, WI, 42.9944°N, 89.4326°W) detected the meteor itself moving toward the horizon. At 15.5 s UTC, the meteor reached the edge of the field of view. Flares are still registered as they lit up the sky and the camera, but the photometry is unreliable past that time. There are seven flares in the video record between 15.9 and 17.2 s UTC. The same flares were detected at SkySentinel node 73 (Grandville, MI, 42.9161°N, 85.7358°W), where the meteor was near, or just outside, the field of view. The pattern of flares is the same in both videos, but Fitchburg is 0.39 s fast compared to Grandville. The reflected light in the Marshall video was aligned in intensity with Fitchburg video and in time with the Grandville video (Fig. 15).

GLM detected two brief flares in the 0.008 s interval at 7:25:17.243–17.251 s and the 0.33 s interval at 7:25:17.337–17.370 s (Fig. 15), coincident with the final orange persistent emission in some of the videos. The most intense GLM-detected flare is only 0.05 s slow compared to the final flare recorded in the Grandville video (Fig. 15, inset). The GLM-derived light curve also has sporadic detections at the ~30 counts/frame level just above the threshold during the 0.8 s interval from 7:25:16.65 to 7:25:17.45 UTC, when SkySentinel cameras recorded several flares (Fig. 15).

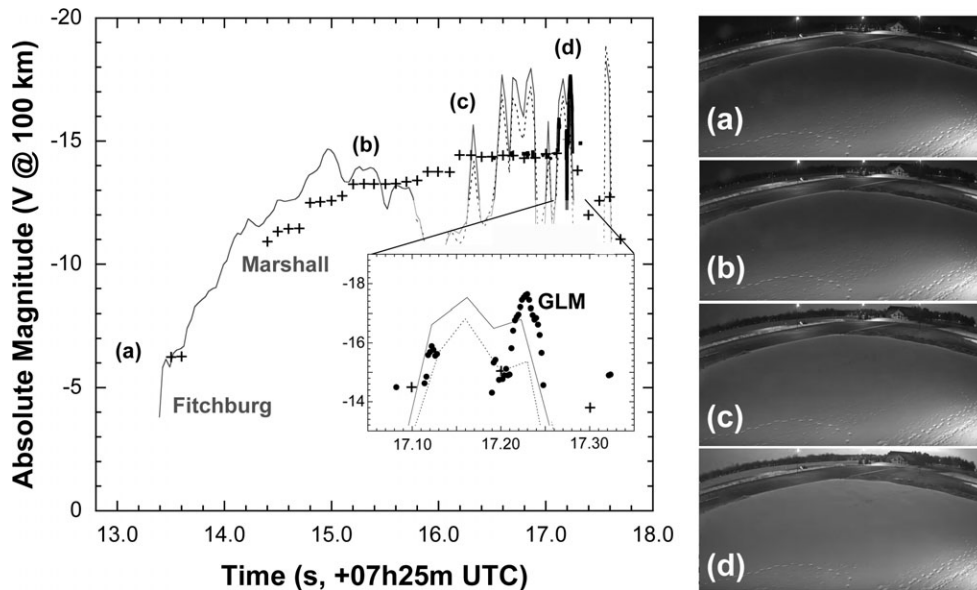


Fig. 15. GLM light curve of the February 06, 2017 Wisconsin fireball, compared to ground-based video data from Fitchburg, WI (solid line) and Grandville, MI (dashed line) and Marshall, WI (+, reflected light). Inset shows an expansion of the data for the period 17.05–17.35 UTC. Right: Marshall, WI, video frames showing brightness of a snow-covered surface (a) prior to the meteor; (b) during plateau; (c) first flare; and (d) most intense flare.

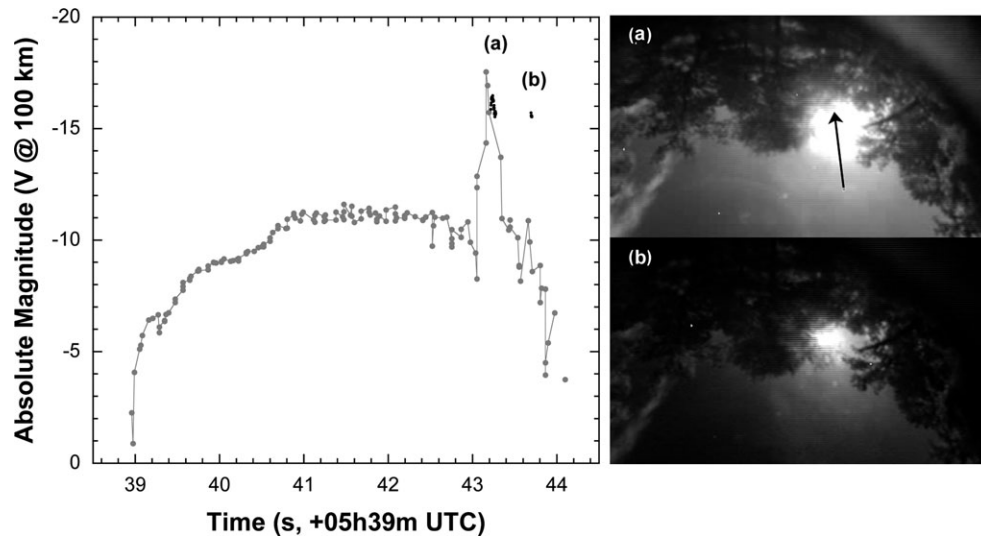


Fig. 16. The May 26, 2017 Lufkin, Texas, meteor light curve, showing GLM data in black and SkySentinel data (adjusted in time by +0.05 s) in gray. Right shows SkySentinel scene from Lufkin at the peak of the two flares.

May 26, 2017: Lufkin

The Lufkin, Texas, meteor is among the faintest bolides captured by GLM so far. The American Meteor Society received 40 reports (fireball 1739-2017). Dash cam video of this fireball exists from police officer Vanzant of the Dallas police department. The air burst was so loud that it rattled doors and windows. People nearby the meteor reported they could see each other briefly as in daylight. SkySentinel station 49 in Lufkin, TX (31.3213°N, 94.8445°W), operated by Ernie Iverson, recorded the meteor in a clear part of the sky (Fig. 16). After the first flare, the meteor is seen to move behind foreground trees.

GLM detected the two flares that lit up the landscape, with SkySentinel times 0.05 s fast compared to those of GLM. The peak count rises just above a 32 counts/frame threshold level, which implies the 1σ noise floor is at 7 (Fig. 16). Again, two brief flares are detected above the threshold level, 0.35 s apart. Level 2 data proved temporally sparser than Level 0 data, suggesting that some threshold event detections were removed.

November 15, 2017: Arizona

The November 15 bolide was reported by 155 observers (AMS fireball 4310-2017). There is no USG detection. SkySentinel detected the bolide from Flagstaff, Arizona

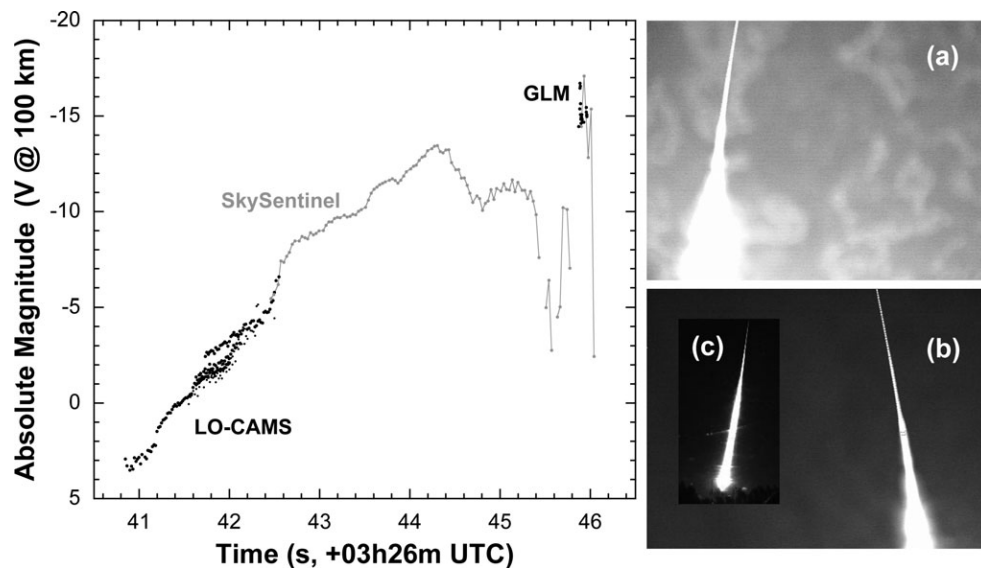


Fig. 17. The November 15, 2017 Arizona fireball, with inset showing LO-CAMS observations from (a) the Discovery Channel Telescope and (b) Lowell Observatory, and (c) allsky observation from Lowell Observatory's Anderson Mesa Station.

(35.203°N, 111.665°W), where it moved behind some trees only after the main flares. The early part was captured by LO-CAMS (Fig. 17), part of the CAMS network with stations at Lowell Observatory and the Discovery Channel Telescope (Jenniskens et al. 2011). Triangulation of the video obtained at these stations (convergence angle $Q = 11.1^\circ$) showed the meteor entered with an apparent speed of $26.03 \pm 0.02 \text{ km s}^{-1}$ moving toward azimuth (from north) $166.9^\circ \pm 0.5^\circ$, with elevation $45.5^\circ \pm 0.8^\circ$. The meteor was first detected at +5 absolute visual magnitude, at an altitude of $104.24 \pm 0.04 \text{ km}$ over $34.7577 \pm 0.0002^\circ\text{N}$, $111.6270 \pm 0.0001^\circ\text{W}$. It left the LO-CAMS camera field of view when it had brightened to an absolute visual magnitude of -3 at an altitude of $77.20 \pm 0.03 \text{ km}$ over $34.5207 \pm 0.0003^\circ\text{N}$, $111.5602 \pm 0.0001^\circ\text{W}$. The calculated orbit is that of an asteroid with semimajor axis of $a = 2.36 \pm 0.04 \text{ AU}$, likely dynamically evolved from an orbit originating in the 3:1 mean motion resonance with Jupiter at $a = 2.5 \text{ AU}$, now having eccentricity $e = 0.597 \pm 0.005$ and high inclination $37.82 \pm 0.08^\circ$. A 60 s exposure on allsky cameras at Anderson Mesa (Fig. 17c) and the Discovery Channel Telescope showed the meteor continued to brighten and produce a flare at $\sim 31 \text{ km}$ altitude just before terminating. No radar signature of falling meteorites was obtained, perhaps because little of this meteoroid survived due to the relatively high entry speed.

GLM detected only the terminal flares. The record shows an initial flare of 240 DN peak intensity, followed by a second flare at 55 DN 0.018 s later and a third flare at 75 DN 0.07 s later. Detail in the light curve is significantly higher than obtained from video records on the ground. Here, SkySentinel times are 0.05 s slow compared to GLM data. Unfortunately, no meteorites have been recovered at the time of writing, so we do not know what type of material entered Earth's atmosphere.

DISCUSSION

Most individual lightning flashes are submillisecond duration, a useful feature to discriminate meteors from lightning (Goodman et al. 1988). Bolide emissions, however, have some resemblance to that of continuing current lightning. Continuing current in cloud-to-ground lightning is a continuous mode of cloud charge transfer to the ground along a lightning channel after a lightning stroke, during which the channel continues to glow (Hagenguth and Anderson 1952). Such lightnings are important as the continuing current contact with a fuel source is a major igniter of forest and wild land fires. Because GLM is designed to capture such continuing current also, all bolides investigated in this study did pass its onboard nonlightning event filters.

Validity of GLM Data for Bolide Research

To make a direct comparison with USG-reported total radiant energies, we took the GLM-detected irradiant energies and calculated what would be “total radiant energy” when making the same assumption about the nature of the bolide emission as in the USG reports. That assumption is that all observed emission is from continuum radiation emitting at 6000 K (Tagliaferri et al. 1998). Figure 18 shows the total radiated energy measured from the reported GLM brightness values (\times) and that corrected for gaps in the light curve and parts of the light curve that were below the detection limit (filled circles). Gray circles show the energy derived from the GLM photometry directly, which assumes that all emission is O I line emission. Solid black circles show the energy if all emission is in continuum radiation instead, with the correction for O I triplet coverage by the pass band removed.

Surprisingly, the calculated total radiant energies (\bullet) correspond within a factor of two to those reported from the USG satellite network, although they tend to be larger for bolides and lower for the smaller fireballs (Table 4). The general agreement implies that the GLM pass band around peak brightness (when most of the energy is emitted) is not dominated by O I line emission, but by the same radiation mechanism that dominates the broadband USG sensor network (Fig. 2), presumably a continuum radiation emitting at 6000 K (or perhaps a representative share of metal atom line emission with a similar overall spectral distribution of energy).

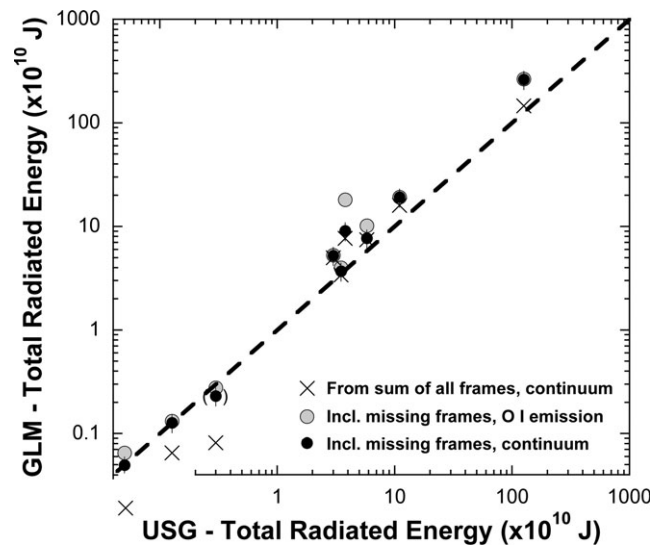


Fig. 18. GLM-derived total radiated energy compared to such information derived from USG satellites. Lowest three points were not reported from USG sensor data (point between brackets has energy estimate from infrasound).

The factor ~ 3 higher radiant energy derived from the British Columbia meteor, which was seen at high angle from nadir, also suggests that the emission in these flares is not dominated by O I atom line emission, but by a form of continuum emission. This would lower the GLM-measured total radiated power by a factor of two (Fig. 11) and bring it more in agreement with the USG-derived values (Fig. 18).

The discrepancy for fireballs with total radiated energy $< 1 \times 10^{10}$ J (~ 0.1 kt yield) may be because much of the energy is emitted during the undetected parts of the meteor light curve. As a result, the GLM-derived total radiated energy appears to be underestimated by a factor of 2–3 for meteors near the detection limit (Fig. 18).

Gaps in the light curve due to FIFO overflow are important for bolides in excess of 30×10^{10} J (Fig. 18), or about 0.4 kt yield, and need to be removed by interpolation. After correction, the GLM-measured intensities tend to be slightly higher than the USG-reported values, perhaps because more of the light curve is sampled due to differences in the detection threshold.

Meteor Physics: O I Line Emission

What fraction of emission in the GLM pass band is O I atom line emission, with wavelengths in vacuum at 777.41, 777.63, and 777.75 nm, depends on the meteor's speed, altitude, and ablation behavior (Popova et al. 2000). The ~ 1.1 nm wide band also covers continuum emission from plasma and dust, a small part of the $\Delta v = +2$ First Positive band system of N_2 , and ablated metal atom emission lines, mainly weak lines with vacuum wavelengths at 777.60 nm (Ti I) and 777.38 nm (Cr I) (NIST database at https://physics.nist.gov/PhysRefData/ASD/lines_form.html and Kurucz tables at https://www.cfa.harvard.edu/ampcgi/read_pac, last accessed 5/2018). The Kurucz tables also list weak lines at 777.52 nm (Fe I), 777.34 and 777.79 nm (Ca I), as well as 777.08 and 777.73 nm (Ti I) (Kurucz and Bell 1995).

Observations of O I Line Emission in Bolides

Excited atomic oxygen is generated via two mechanisms during atmospheric entry. First, molecular oxygen in the atmosphere is dissociated and excited as it passes through the strong shockwave just ahead of the meteoroid. Second, ablation products, in the form of metallic oxides, have low dissociation energies, and can further increase the abundance of atomic oxygen in the wake. Oxygen is the most abundant element in stony meteoroids.

Most radiated emission in a bright meteor is from this bow shock, where temperatures are of order 10,000 K, and from a warm plasma immediately behind the meteoroid, where electronic excitation temperatures are typically of order 3500–6500 K (Ceplecha 1971;

Borovicka 1993; Jenniskens et al. 2004). After passing over any given GLM pixel, the plasma quickly cools and fades (a phase called “afterglow,” which includes molecular band emissions of CaO, etc.), followed by a ~ 30 s period of line emission due to recombination (and forbidden line emission of oxygen) (Borovicka and Jenniskens 2000). Following that is an even fainter persistent yellow chemiluminescence from mostly FeO radicals that can last for tens of seconds to many minutes (Jenniskens et al. 2000a).

Fast meteors have strong O I emission lines (Jenniskens et al. 2000b). Some spectra of bright fast meteors have been captured serendipitously by large telescopes, providing highly resolved spectra (Jehin et al. 2007; Passas et al. 2016). Model spectra compared to these data show that the First Positive band of N_2 correlates with the strength of the O I line emission and is only a minor $< 5\%$ contributor to the GLM pass band (Jehin et al. 2007).

Meteors brighter than absolute visual magnitude -13 , however, tend to be asteroids in short-period orbits that enter at a slow < 35 km s^{-1} speed (Brown et al. 2016). Fainter meteors of that speed tend to have weak O I lines, only 10% of the brightest Mg I lines (Vojacek et al. 2015). Even bright fireballs, such as the -19.5 magnitude *Benesov* bolide, are dominated by metal atom emission lines Fe I, Mg I, Na I, Ca I, etc. (Borovicka and Bereznoy 2016). If metal atom lines dominate the 777.4 nm wavelength pass band of GLM, they are detected with an efficiency dependence on angle from nadir other than that for O I.

O I atom line emission is also proportionally less important during flares, when fragmentation processes suddenly produce a large surface area of small meteoroid particles. Unfortunately, most past bolide spectra of flares were obtained by spectrographs not sensitive beyond 660 nm (Ceplecha 1964). However, photographic spectra do detect O I at 615.60–82 nm. Weak emission at that position was identified as the 615.44 Na I line (Ceplecha and Rajchl 1963; Ceplecha 1966). In addition, a highly dispersed 32.6 km s^{-1} magnitude -12.4 meteor spectrum of flares showed only weak O I lines, dominated by the nearby resolved 616.13–22 nm emission of Ca I (Ceplecha 1971).

In comparison, Taylor et al. (2007) detected strong continuum emission in fast Leonids at 960–1640 nm, while Borovicka et al. (1999) estimated that 1/6 of radiation was emitted in a thermal continuum in faint video-detected Leonids. Continuum emission from recondensed vapor is prominent at 777 nm in laboratory experiments of meteor ablation (Milley et al. 2007).

Model of O I Line Emission in Bolides

To gain further insight into the expected O I emission of meter-sized asteroid entries in Earth's

atmosphere, chemically reacting computational fluid dynamics simulations were performed, with coupled ablation and radiative transport, using the methodology detailed in Johnston et al. (2018). For the purpose of this discussion, a 2 m diameter spherical meteoroid of LL chondrite composition for elements O (relative abundance 0.457), Si (0.206), Fe (0.172), Mg (0.120), Na (0.005), S (0.020), Al (0.010), and Ca (0.010), moving at 20 km s^{-1} in air representative for altitudes of 60, 50, 40, and 30 km were considered. Spectra within the 777.6–778.0 nm wavelength range of the GLM sensor were computed as detected by an observer at a distance of 100 km from the meteoroid.

Figure 19 shows the computed radiant flux. O I line emission is expected even at 30 km altitude, both from the shockwave and the warm wake immediately behind the meteoroid. Fe and Ca lines do not significantly contribute. The apparent continuum background in these spectra originates from Stark line broadening, as well as free-free and bound-free transitions in the high-temperature plasma (Fig. 19, lower diagram). Continuum emission from free-free transitions is proportional to the electron number density, which for large meteoroids can be quite large. The meteoroid surface also emits a continuum blackbody radiation, however, due to the optical thickness of the shocked air and ablation products, as well the relatively small surface area of the meteoroid compared with the radiating gas volume, its contribution to the observed spectrum within the GLM pass band is negligible.

The majority of emission from these sources originates from the shock layer and the near-wake (<2 meteoroid diameters downstream). The meteoroid itself shields much of the stagnation point area at the large viewing angles, the angle from which the meteor is observed relative to the direction of motion. Even at larger viewing angles, part of the shockwave and warm wake remain visible (Fig. 20). As a result, the relative contribution of O I emission is higher in the larger viewing angles of space-borne observations compared to ground-based observations.

Seen from 90° viewing angle, the total irradiance increased exponentially from $0.45 \times 10^{-4} \text{ W m}^{-2} \text{ nm}^{-1}$ at 60 km (corresponding to an absolute visual magnitude $m_V = -15.1$ magnitude) to $1.9 \times 10^{-4} \text{ W m}^{-2} \text{ nm}^{-1}$ at 30 km altitude ($m_V = -16.7$). Lower in the atmosphere, where pressures are higher, the relative contribution of free-free and bound-free emission and the Stark broadening effect of the O I lines increases. The fraction of continuum relative to the narrow O I line emission increases with decreasing altitude, but does not exceed 40% of the total radiance at altitudes above 30 km.

Three dashed and solid curves in Fig. 4 depict this calculated altitude-dependence, each curve showing the

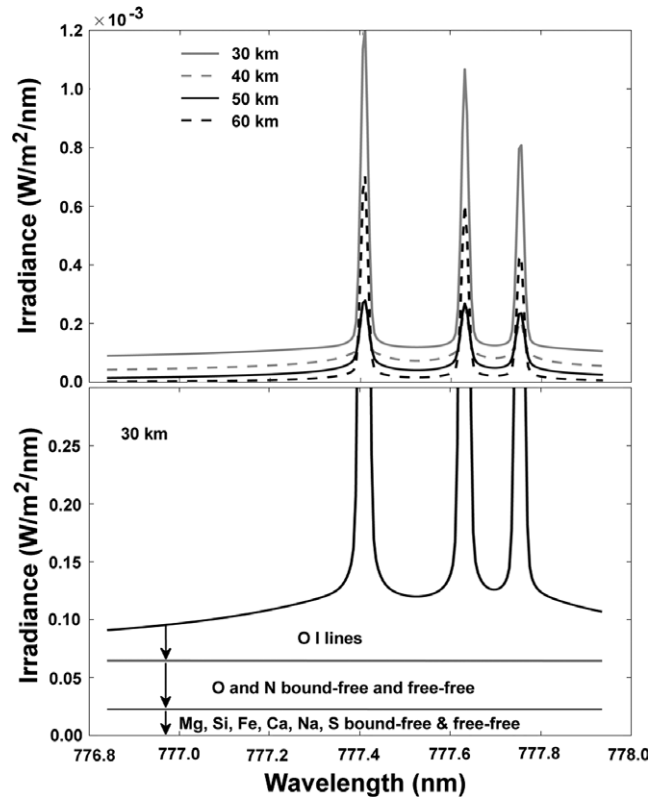


Fig. 19. Calculated spectral irradiance of meteor plasma as seen from a 100 km distance for a 2 m sized meteoroid moving at 20 km s^{-1} in air representative for altitudes of 30–60 km.

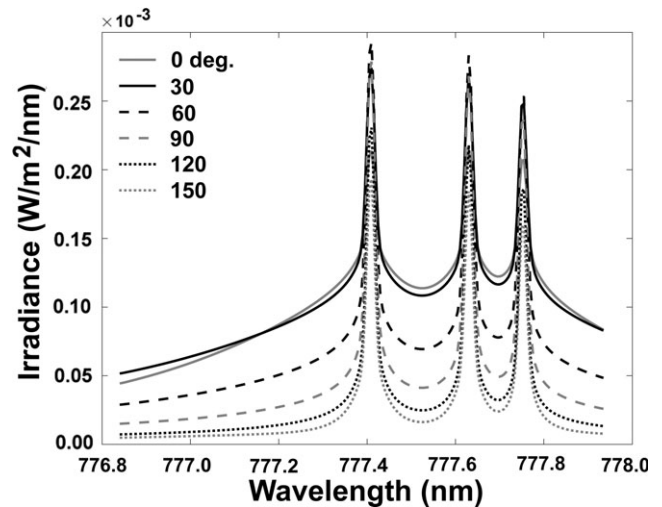


Fig. 20. As Fig. 19, but shown as a function of viewing angle relative to direction of motion.

time evolution expected for different entry speeds in a vertical angle of incidence. Vertical dashes mark the corresponding altitude, if peak brightness is at 28 km altitude. The thick solid line was fitted to an early part of the light curve that has the expected slope. There

appear to have been flares in the light curve, probably caused by fragmentation, at times 20.0, 21.0, and 21.5 s. The theoretical thick solid line in Fig. 4 corresponds well with the bolide brightness increase when the flares are excluded. This line, corresponding to 20 km s^{-1} at 0° angle of incidence, would have the bolide's beginning altitude at about 72 km. If the meteor moved faster or slower than this line, this would imply that the meteor's beginning altitude was higher or lower, respectively.

Compared to our calculated dependence of O I emission on altitude, the West Atlantic bolide shows a rapid onset of emission at 19.62 s, which is incompatible with the expected gradual formation of the shock wave, or even with the meteoroid gradually becoming hot enough to radiate continuum emission at 777 nm. Instead, this point in time may represent the moment the meteoroid becomes hot enough to ablate. At that point, we surmise that metal oxides from ablating silicates start contributing to the creation of O I atoms.

Following this rapid onset is an altitude-dependence expected if the observed luminosity is proportional to atmospheric density, steeper than expected from O I line emission alone. From 19.90 to 20.19 s, the irradiance increases exponentially with an exponent 0.502 s^{-1} (gray line in Fig. 4). It is possible that loose material is sloughing off the meteoroid and we are seeing a form of ablation not included in the model. The slope of the line implies that the vertical component of the velocity vector is 8.7 km s^{-1} (assuming an atmospheric density profile as in the 1976 US Standard Atmosphere). The projected speed of the meteoroid on the lightning ellipsoid (4.3 pixels in 2.055 s) is 17.1 km s^{-1} .

At 20.190 s, the emission starts to decrease until settling at a plateau that has the altitude-dependence expected for O I line emission. During this time, O I line emission may dominate the irradiance.

If much of the meteoroid remains intact leading up to the peak, the O I shock emission does not contribute significantly to the bolide's peak emission in the GLM pass band. At 20.71 s, intensity increases to a level expected if ablation again dominated the emission, perhaps signifying fragmentation. There are sharp irregularities in the light curve that may be diagnostic. At 21.71 s, an increase of luminosity starts that is even more rapid than expected from the atmospheric density alone, which leads up to the main peak.

Again, the situation could be different for fast (cometary) meteoroids. The 72 km s^{-1} fast Leonids, for example, are known to have strong O I line emission, although in flares metal atom line emission dominated (e.g., Millman and Halliday 1961; Borovicka and Bocek 1995). Most meteor showers contain only meteors fainter than -13 magnitude, but the 31 km s^{-1} fast Taurids are known to contain bolides (Jenniskens 2006).

Implications for the Analysis of Past Bolide Light Curves

The USG-derived values for the velocity vector of the British Columbia meteor in an Earth-fixed reference frame ($V_x = -12.7$, $V_y = -6.1$, and $V_z = -4.2 \text{ km s}^{-1}$) translate to a direction toward $Az = 280.1^\circ$, $El = 13.3^\circ$. In contrast, the ground-based video-derived (and GLM confirmed) observed values differ by $\sim 77^\circ$ in azimuth and $\sim 23^\circ$ in elevation (Hildebrand, personal communication). Similar large discrepancies between USG-reported direction and speed and that measured from the ground were noticed before (Borovicka et al. 2017).

These large discrepancies caution the use of USG sensor astrometry alone for trajectory reconstruction. This could explain, for example, why the -21.4 magnitude 1997 Greenland superbolide (Table 1) was determined to be in a long-period comet orbit based on USG sensor astrometry, but composed of strong enough material to penetrate to 25 km altitude in the atmosphere with a low value of the ablation coefficient (Pedersen et al. 2001).

A future comparison of USG-sensor and GLM-detected bolide light curves may shed light on the ablation and fragmentation properties of meteoroids. The ground-based video of the L5 ordinary chondrite Park Forest (Table 1), for example, showed similar differences with USG space-based observations (Brown et al. 2004) than seen here for the case of the British Columbia meteor. The main flare at 37 km altitude was more prominent in USG data than in ground-based video compared to other flares earlier and later. This behavior can be due to unfortunate instrumental effects such as saturation in the videos, or due to favorable differences in spectral responsivity of the sensors if the main peak is a more prominent emitter at the near-IR wavelengths detected by USG sensors, compared to the R, G, and B visible bands of video cameras (Fig. 2).

The published USG sensor light curves cover a wide range of material types. Notably, the C2 carbonaceous chondrite Tagish Lake (Table 1) represents the lowest strength end of the carbonaceous chondrite range (type II bolides) in the classification system of Ceplecha (1988). The light curve was surprisingly smooth over its >5 s duration (Brown et al. 2002c), similar in shape and smoothness to that of the GLM-detected bolide off Baja California discussed here, except that light curve evolved at a speed five times faster. Such similarities may help understand the influx of materials that do not readily survive to the ground.

Future Work

Because of its global coverage and many years of operations, the USG-sensor data represent a unique

data set of bolide light curves that is not soon replaced by GLM data or any other type of observations. Over time, however, the GLM coverage will increase. GLM presently covers a fraction 0.26 of Earth, but future sensors are expected to add to that. There are four satellites in the GOES series, with GOES-R and GOES-S launched by the time of this publication, while GOES-T and GOES-U are in production. In December 2017, GOES-R (now GOES-16) became GOES-East, after the spacecraft was repositioned in geostationary orbit to 75.2°W. GOES-S will be renamed GOES-17 and positioned over 137°W. Together, GOES-16 and GOES-17 will cover the longitude range from about 18°W to 195°W (165°E), covering both the Pacific and the Atlantic Oceans and North and South America with some overlap, and about one-third of the globe.

A future effort may include the development of automatic detection of bolides in GLM data, for example, by looking for extended duration events over sea or land with no cloud cover. This may lead to a new Level 2a product that would retain the lowest intensity resolution in energy and provide corrected energies and geolocations. For bolides observed in the overlapping area of GOES-16 and GOES-17, the stereo astrometry may be used to derive full solutions for the bolide trajectory and speed by triangulation, for bolides more intense than about 0.2 kt.

CONCLUSIONS

The practical use of the GLM for the detection of meteoroid impacts, foreseen by Tagliaferri et al. (1998) 20 years ago, has now been demonstrated. Based on our exploratory work, GLM is able to detect bolides of absolute visual magnitude (seen from 100 km distance) of about -14 magnitude in nighttime and about -15 magnitude in daytime. The sensitivity drops slightly toward higher angles from nadir. This makes GLM capable of monitoring the impact of several decimeter- to several meter-sized asteroids in Earth's atmosphere, revealing a variety of fragmentation behavior. GLM is not expected to detect meteor showers well, because most contain only meteors fainter than -13 magnitude, but there are exceptions.

GLM Level 0 data sample the light curve of bolides nearly completely above the threshold limit. Onboard processes create a background drift that can be removed to good effect with the Level 0 data that are being down-linked. Small gaps in the light curve at peak brightness for impacts larger than 0.14 kt are caused by the transient event count exceeding a maximum value for each downlink unit, but those gaps typically have little negative impact on the interpretation of the light curve data.

The current Level 2 data suffer from discretization at the lowest intensity levels, making it difficult to remove the background variation over the duration of the bolide. The Level 2 product also filters out some events and groups others in ground processing, which removes temporal resolution in some of the light curves.

The good agreement between calculated total radiant energy from narrow-band GLM data and broadband USG data implies that bolide emission at peak brightness is dominated by continuum radiation rather than O I line emission. Model calculations confirm that the expected O I line emission intensity does not increase as rapidly toward peak brightness than the observed total flux. The GLM flux is corrected for shifts in the central wavelengths of the pass bands, which determine the amount of O I line emission observed, but do not affect the continuum emission. As a result, the reported flux levels are overestimated by up to 20% within 7° from nadir, but more so for the larger ~ 7 – 8° angles.

GLM data also support USG-sensor information by providing a verification of astrometric information and by adding light curves in a different (much more narrow) wavelength pass band. Comparison of USG and GLM light curves for the same bolides may reveal additional insights into light emission mechanisms of bolides. The chemistry and spectroscopic properties of oxygen are well studied due to its engineering importance for spacecraft entry. Especially the narrow-band GLM data from the early part of the brightest impacts have the potential to be a cleaner data source for the development and validation of models for meteoroid entry.

GLM sensors, albeit specifically designed for lightning detection and mapping, are expected to contribute useful bolide light curves in the next 20 years. That data may lead to a better understanding of what type of meter-sized asteroids impact Earth's atmosphere and how materials from different source regions in the asteroid belt fragment in Earth's atmosphere, as well as fill gaps in the current global bolide monitoring system of systems.

Acknowledgments—We thank Jessie Dotson and David Morrison for a careful reading of the manuscript and helpful comments. A. H., L. H., F. C., and D. H. acknowledge timely fieldwork support from the University of Calgary for the British Columbia meteorite fall, with special appreciation to security camera owners R. Goodwin, D. MacCallum, R. Bateman, the Ainsworth Hotsprings Resort, and the Canadian Forest Products Ltd., as well as to the Summit Lake dash cam owner M. Stevenson. P. J., E. S., C. J., and R. L. are supported by the Asteroid Threat Assessment Project at NASA Ames Research Center. NASA's Planetary Defense Coordination Office (PDCO) funded this work. The paper was made

possible also in part by work performed under NASA contract NNGO8HZOOC. The views, opinions, and findings contained in this report are those of the authors and should not be construed as an official National Oceanic and Atmospheric Administration or U.S. government position, policy, or decision.

Editorial Handling—Dr. Josep M. Trigo-Rodríguez

REFERENCES

- Borovička J. 1993. A fireball spectrum analysis. *Astronomy & Astrophysics* 279:627–645.
- Borovička J. 2005. Spectral investigation of two asteroid fireballs. *Earth, Moon, and Planets* 97:279–293.
- Borovička J. and Berezhnoy A. A. 2016. Radiation of molecules in Benesov bolide spectra. *Icarus* 278:248–265.
- Borovička J. and Bocek J. 1995. Television spectra of meteors. *Earth, Moon, and Planets* 71:237–244.
- Borovička J. and Charvát Z. 2009. Meteorite observation of the atmospheric entry of 2008 TC3 over Sudan and the associated dust cloud. *Astronomy & Astrophysics* 507:1015–1022.
- Borovička J. and Jenniskens P. 2000. Time resolved spectroscopy of a Leonid fireball afterglow. *Earth, Moon, and Planets* 82:399–428.
- Borovička J., Stork R., and Bocek J. 1999. First results from video spectroscopy of 1998 Leonid meteors. *Meteoritics & Planetary Science* 34:987–994.
- Borovička J., Spurný P., Kalenda P., and Tagliaferri E. 2003. The Morávka meteorite fall: I. Description of the events and determination of the fireball trajectory and orbit from video records. *Meteoritics & Planetary Science* 38:975–987.
- Borovička J., Spurný P., Grigore V. I., and Svoren J. 2017. The January 7, 2015, superbolide over Romania and structural diversity of meter-sized asteroids. *Planetary and Space Science* 143:147–158.
- Brown P., Hildebrand A. R., Green D. W., Pagé D., Jacobs C., ReVelle D., Tagliaferri E., Wacker J., and Wetmiller B. 1996. The fall of the St-Robert meteorite. *Meteoritics & Planetary Science* 31:502–517.
- Brown P. G., Spalding R. E., ReVelle D. O., Tagliaferri E., and Worden S. P. 2002a. The flux of small near-Earth objects colliding with the Earth. *Nature* 420:294–296.
- Brown P. G., Whitaker R. W., ReVelle D. O., and Tagliaferri E. 2002b. Multi-station infrasonic observations of two large bolides: Signal interpretation and implications for monitoring of atmospheric explosions. *Geophysical Research Letters* 29:14-1–14-4.
- Brown P. G., ReVelle D. O., Tagliaferri E., and Hildebrand A. R. 2002c. An entry model for the Tagish Lake fireball using seismic, satellite and infrasound records. *Meteoritics & Planetary Science* 37:661–675.
- Brown P., Pack D., Edwards W. N., ReVelle D. O., Yoo B. B., Spalding R. E., and Tagliaferri E. 2004. The orbit, atmospheric dynamics, and initial mass of the Park Forest meteorite. *Meteoritics & Planetary Science* 39:1781–1796.
- Brown P. G., Assink J. D., Astiz L., Blaauw R., Boslough M. B., Borovička J., Brachet N., Brown D., Campbell-Brown M., Ceranna L., Cooke W., De Groot-Hedlin C., Drob D. P., Edwards W., Evers L. G., Garces M., Gill J., Hedlin M., Kingery A., Laske G., Le Pichon A., Mialle P., Moser D. E., Saffer A., Silber E., Smets P., Spalding R. E., Spurný P., Tagliaferri E., Uren D., Weryk R. J., Whitaker R., and Krzeminski Z. 2013. A 500-kiloton airburst over Chelyabinsk and an enhanced hazard from small impacts. *Nature* 503:238–241.
- Brown P., Wiegert P., Clark D., and Tagliaferri E. 2016. Orbital and physical characteristics of meter-scale impactors from airburst observations. *Icarus* 266:96–111.
- Buechler D. E., Koshak W. J., Christian H. J., and Goodman S. J. 2014. Assessing the performance of the Lightning Imaging Sensor (LIS) using deep convective clouds. *Atmospheric Research* 135–136:397–403.
- Ceplecha Z. 1964. Study of a bright meteor flare by means of emission curve of growth. *Bulletin of the Astronomical Institute of Czechoslovakia* 15:102–112.
- Ceplecha Z. 1966. Complete data on iron meteoroid (Meteor 36221). *Bulletin of the Astronomical Institute of Czechoslovakia* 17:195–206.
- Ceplecha Z. 1971. Spectral data on terminal flare and wake of double-station meteor No. 38421 (Ondrejov, April 21, 1963). *Bulletin of the Astronomical Institute of Czechoslovakia* 22:219–304.
- Ceplecha Z. 1988. Earth's influx of different populations of sporadic meteoroids from photographic and television data. *Bulletin of the Astronomical Institute of Czechoslovakia* 39:221–236.
- Ceplecha Z. and Rajchl J. 1963. Meteor spectra with high dispersion. *Smithsonian Contributions to Astrophysics* 7:129–153.
- Ceplecha Z., Spalding R. E., Jacobs C., ReVelle D. O., Tagliaferri E., and Brown P. 1999. Superbolides. In *Meteoroids 1998*, edited by Baggaley W. J. and Porubcan V. Stará Lesná, Slovakia: Astronomical Institute of the Slovak Academy of Sciences. pp. 37–54.
- Christian H. J. and Goodman S. J. 1987. Optical observations of lightning from a high-altitude airplane. *Journal of Atmospheric and Oceanic Technology* 4:701–711.
- Christian H. J., Blakeslee R. J., and Goodman S. J. 1989. The detection of lightning from geostationary orbit. *Journal of Geophysical Research* 94:13,329–13,337.
- Clark D. 2017. Infrasound yield estimate provided in news media reports. NASA Watch the Skies blog. January 18. https://blogs.nasa.gov/Watch_the_Skies
- Ens T. A., Brown P. G., Edwards W. N., and Silber E. A. 2012. Infrasound production by bolides: A global statistical study. *Journal of Atmospheric and Solar-Terrestrial Physics* 80:208–229.
- Fries M., Fries J., Hankey M., and Matson R. 2016. Meteorite falls observed in U.S. weather radar data in 2015 and 2016 (to date). 79th Meteoritical Society meeting, Berlin, Germany. Abstract. 1 p.
- Gi N. and Brown P. 2017. Refinement of bolide characteristics from infrasound measurements. *Planetary and Space Science* 143:169–181.
- GOES-R Data Book 2018. Greenbelt, Maryland: NASA Goddard Space Flight Center.
- Goodman S. J., Christian H. J., and Rust W. D. 1988. A comparison of the optical pulse characteristics of intracloud and cloud-to-cloud lightning as observed above clouds. *Journal of Applied Meteorology* 27:1369–1381.
- Goodman S. J., Blakeslee R. J., Koshak W. J., Mach D., Bailey J., Buechler D., Carey L., Schultz C., Bateman M., McCaul E. Jr., and Stano G. 2013. The GOES-R Geostationary Lightning Mapper (GLM). *Atmospheric Research* 125:34–49.
- Hagenguth J. H. and Anderson J. G. 1952. Lightning to the Empire building Part III. *Journal of the American Institute of Electrical Engineers* 71:641–649.

- Hildebrand A. R., McCausland P. J. A., Brown P. G., Longstaffe F. J., Russell S. D. J., Tagliaferri E., Wacker J. F., and Mazur M. J. 2006. The fall and recovery of the Tagish Lake meteorite. *Meteoritics & Planetary Science* 41:407–431.
- Jehin E., Jenniskens P., Cabarnac R. A., Laux C. O., and Boyd I. D. 2007. Spectroscopic anatomy of a meteor with the very large telescope (ESO). *Advances in Space Research* 39:550–554.
- Jenniskens P. 2006. *Meteor showers and their parent comets*. Cambridge, UK: Cambridge University Press. 790 p.
- Jenniskens P., Lacey M., Allan B. J., Self D. E., and Plane J. M. C. 2000a. FeO “orange arc” emission detected in optical spectrum of Leonid persistent train. *Earth, Moon, and Planets* 82:429–438.
- Jenniskens P., Wilson M. A., Packan D., Laux C. O., Krüger C. H., Boyd I. D., Popova O. P., and Fonda M. 2000b. Meteors: A delivery mechanism of organic matter to the early Earth. *Earth, Moon, and Planets* 82:57–70.
- Jenniskens P., Laux C. O., Wilson M. A., and Schaller E. L. 2004. The mass and speed dependence of meteor air plasma temperatures. *Astrobiology* 4:81–94.
- Jenniskens P., Gural P. S., Dynneson L., Grigsby B. J., Newman K. E., Borden M., Koop M., and Holman D. 2011. CAMS: Cameras for Allsky Meteor Surveillance to establish minor meteor showers. *Icarus* 216:40–61.
- Jenniskens P., Rubin A. E., Yin Q.-Z., Sears D. W. G., Sandford S. A., Zolensky M. E., Krot A. N., Blair L., Kane D., Utas J., Verish R., Friedrich J. M., Wimpenny J., Eppich G. R., Ziegler K., Verosub K. L., Rowland D. J., Albers J., Gural P. S., Grigsby B., Fries M. D., Matson R., Johnston M., Silber E., Brown P., Yamakawa A., Sanborn M. E., Laubenstein M., Welten K. C., Nishiizumi K., Meier M. M. M., Busemann H., Clay P., Caffee M. W., Schmitt-Kopplin P., Hertkorn N., Glavin D. P., Callahan M. P., Dworkin J. P., Wu Q., Zare R. N., Grady M., Verchovsky S., Emel'yanenko V., Naroenkov S., Clark D. L., Girten B., and Worden P. S. 2014. Fall, recovery and characterization of the Novato L6 chondrite breccia. *Meteoritics & Planetary Science* 49:1388–1425.
- Johnston C. O., Stern E. C., and Wheeler L. F. 2018. Radiative heating of large meteoroids during atmospheric entry. *Icarus* 309:25–44.
- Klekociuk A. R., Brown P. G., Pack D. W., ReVelle R. O., Edwards W. N., Spalding R. E., Tagliaferri E., Yoo B. B., and Zagari J. 2005. Meteoritic dust from the atmospheric disintegration of a large meteoroid. *Nature* 436:1132–1135.
- Konovalova N. A., Madiedo J. M., and Trigo-Rodríguez J. M. 2013. The Tajikistan superbolide of July 23, 2008. I. Trajectory, orbit, and preliminary fall data. *Meteoritics & Planetary Science* 48:2469–2479.
- Koshak W. J., Stewart M. F., Christian J. J., Bergstrom J. W., Hall J. M., and Solakiewicz R. J. 2000. Laboratory calibration of the optical transient detector and the lightning imaging sensor. *Journal of Atmospheric and Oceanic Technology* 17:905–915.
- Kurucz R. L. and Bell B. 1995. 1995 Atomic Line Data, Kurucz CD-ROM No. 23. Cambridge, Massachusetts: Smithsonian Astrophysical Observatory.
- Mach D., Christian H., Blakeslee R., Boccippio D., Goodman S., and Boeck W. 2007. Performance assessment of the optical transient detector and lightning imaging sensor. Part II: Clustering algorithm. *Journal of Geophysical Research* 112:D09210. <https://doi.org/10.1029/2006JD007787>.
- McCord T. B., Morris J., Persing D., Tagliaferri E., Jacobs C., Spalding R., Grady L., and Schmidt R. 1995. Detection of a meteoroid entry into the Earth's atmosphere on February 1, 1994. *Journal of Geophysical Research* 100:3245–3249.
- Miller S. D., Straka W. C., Bachmeier A. S., Schmit T. J., Partain P. T., and Noh Y.-J. 2013. Earth viewing satellite perspectives on the Chelyabinsk meteor event. *Proceedings of the National Academy of Sciences* 110:18,092–18,097.
- Milley E. P., Hawkes R. L., and Ehrman J. M. 2007. Meteor luminosity simulation through laser ablation of meteorites. *Monthly Notices of the Royal Astronomical Society* 382: L67–L71.
- Millman P. M. and Halliday I. 1961. The near-infra-red spectrum of meteors. *Planetary and Space Science* 5:137–139.
- Nemtchinov I. V., Svetsov V. V., Kosarev I. B., Golub' A. P., Popova O. P., Shuvalov V. V., Spalding R. E., Jacobs C., and Tagliaferri E. 1997. Assessment of kinetic energy of meteoroids detected by satellite-based light sensors. *Icarus* 130:259–274.
- Passas M., Madiedo J. M., and Gordillo-Vázquez F. J. 2016. High resolution spectroscopy of an Orionid meteor from 700 to 800 nm. *Icarus* 266:134–141.
- Pedersen H., Spalding R. E., Tagliaferri E., Cepelcha Z., Risbo T., and Haack H. 2001. Greenland superbolide event of 1997 December 9. *Meteoritics & Planetary Science* 36:549–558.
- Popova O. P., Sidneva S. N., Shuvalov V. V., and Strelkov A. S. 2000. Screening of meteoroids by ablation vapor in high-velocity meteors. *Earth, Moon, and Planets* 82:109–128.
- Rafal M., Clarke J. T., and Cholvibul R. W. 2016. Post launch calibration and testing of the Geostationary Lightning Mapper on GOES-R Satellite. *Proceedings of the SPIE, Volume 9881*. <https://doi.org/10.1117/12.2228540>
- Register P. J., Mathias D. L., and Wheeler L. F. 2017. Asteroid fragmentation approaches for modeling atmospheric energy deposition. *Icarus* 284:157–166.
- Sigernes F., Peters N., Dyrland M., and Kosch M. 2009. The absolute sensitivity of digital colour cameras. *Optics Express* 17:20,211–20,220.
- Tagliaferri E., Spalding R., Jacobs C., and Cepelcha Z. 1995. Analysis of the Marshall Islands fireball of February 1, 1994. *Earth, Moon, and Planets* 68:563–572.
- Tagliaferri E., Spalding R., Jacobs C., and Erlich A. 1998. Detection of meteoroid impacts by optical sensors in Earth orbit. In *Hazards due to comets and asteroids*, edited by Gehrels T., Matthews M. S., and Schumann A. Tucson, Arizona: The University of Arizona Press. pp. 199–220.
- Taylor M. J., Jenniskens P., Nielsen K., and Pautet D. 2007. First 0.96–1.46 micron near-IR spectra of meteors. *Advances in Space Research* 39:544–549.
- Vojacek V., Borovicka J., Koten P., Spurny P., and Stork R. 2015. Catalogue of representative meteor spectra. *Astronomy & Astrophysics* 580:A67–98.
- Wheeler L. F., Register P. J., and Mathias D. L. 2017. A fragment-cloud model for asteroid breakup and atmospheric energy deposition. *Icarus* 295:149–169.
- Yang J., Messinger D. W., Dube R. R., and Lentilucci E. J. 2017. Fixed pattern noise pixel-wise linear correction for crime scene imaging CMOS sensor. *Proceedings of the SPIE, Volume 10198*. <https://doi.org/10.1117/12.2262035>